# Rupture processes of large deep-focus earthquakes from inversion of moment rate functions

Michael Antolik[1], Douglas Dreger, and Barbara Romanowicz

Seismological Laboratory, University of California, Berkeley

**Abstract.** We determine the source time histories of five recent (1994-1996) large, deep-focus earthquakes using a method that inverts for fault slip from far-field moment rate functions. The moment rate functions are obtained through the deconvolution of multiple body wave phases using broadband records from Global Seismic Network (GSN) and GEOSCOPE stations. Tests of this method on synthetic data indicate that it is successful in determining the low-frequency rupture charactersitics of deep earthquakes under a variety of complicating conditions. We find that source parameters such as average rupture velocity and stress drop are highly variable among the events studied and that some unusual characteristics exhibited by the June 9, 1994, great Bolivian earthquake are also found for other events. Comparison of the slip distributions with background seismicity and aftershock locations indicates that most of the moment release for large deep-focus earthquakes is probably occurring within the active slab interior. This provides further evidence that temperature-controlled mechanisms (such as transformational faulting) play a large role in deep earthquake faulting. Most of the events studied also show a tendency for horizontal rupture propagation, suggesting that isobaric processes may be an important factor in controlling progression of the rupture. Large gaps in the slip distributions point to possible occurrence on multiple fault planes.

## 1. Introduction

The physical mechanism responsible for the occurrence of deep-focus earthquakes has received much renewed attention in the last few years, mainly because of the occurrence of several rare, very large events such as the March 9, 1994 Fiji Islands earthquake ($M_w$ 7.6) and the June 9, 1994, Bolivia earthquake ($M_w$ 8.3). The recent proliferation of high-quality, broadband data from the Global Seismic Network as well as various regional networks has allowed these two ruptures to be examined in considerable detail [*Silver et al.*, 1995; *Goes and Ritsema*, 1995; *McGuire et al.*, 1997; *Estabrook and Bock*, 1995; *Ihmlé*, 1998]. As a result of some of these studies, the favored hypothesis that most deep events are the result of transformational faulting in olivine has become seriously questioned [*Stein*, 1995; *Houston*, 1994]. The total dimensions of both the Fiji (~50 x 30 km²) and Bolivia events (~60 x 40 km²) far exceed the dimensions expected for a wedge of metastable olivine existing in

the cold interior of subducted slabs at depths of ~600 km [see *Kirby et al.*, 1991]. Furthermore, both of these events appear to have ruptured completely through the seismically active portions of the slab as determined by previous background seismicity and the aftershock distributions [*Wiens et al.*, 1994; *Myers et al.*, 1995].

The Bolivia earthquake exhibited other unusual characteristics. For example, the main moment release was preceded by a small-amplitude precursor of ~10 s duration. This precursor appears in many ways to be similar to an ordinary foreshock [*Kikuchi and Kanamori*, 1994] but was separated from the main portion of the rupture by 25 km. Little or no slip appears to have occurred in the intervening space [*Antolik et al.*, 1996]. The earthquake was also characterized by an extremely small average rupture velocity ($< 2.0$ km s$^{-1}$) that likely persisted throughout the duration of the rupture. Much of the slip was concentrated in a very small area, leading to very high estimates of the static stress drop (40 to nearly 300 MPa). The Fiji Islands earthquake, on the other hand, appears to be similar to shallow earthquakes with more normal estimates of the stress drop and rupture velocity.

Accurate resolution of the source characteristics is obviously a very important factor in the selection of possible candidate mechanisms for deep earthquake occurrence (see *Frohlich* [1989] for a review of proposed mechanisms). Up until now, lack of high-quality data

---

[1]Now at Department of Earth and Planetary Sciences, Harvard University, Cambridge, Massachusetts 02138.

has made such resolution difficult at best. Probably the best determined source characteristic of deep earthquakes is their relatively short duration [*Vidale and Houston*, 1993]. Low amounts of seismic energy release have also been observed [*Vassiliou and Kanamori*, 1982]. Although the static stress drop of deep-focus events is generally considered to be higher than that for shallow earthquakes, the amount of uncertainty is considerable [e.g., *Chung and Kanamori*, 1980]. Most studies of the spatial distribution of moment release have concentrated mainly on the locations of asperities relative to the hypocenter [e.g., *Fukao and Kikuchi*, 1987; *Willemann and Frohlich*, 1987] rather than recovery of the actual slip distribution. Thus to what extent moment release occurs outside the cold core of subducted slabs has remained largely unknown. Aftershock locations generally do not provide an adequate indication of the source dimensions [*Frohlich*, 1987]. The causative fault planes for most deep events prior to 1994 have not been resolved, although *Lundgren and Giardini* [1992] have attempted to link lineations in deep earthquake hypocenters with nearby rupture planes.

Our objective in this paper is to examine the rupture characteristics of some of the other large deep-focus earthquakes occurring within the past 3 years in order to determine how characteristic the well-determined source properties of the Fiji Island and Bolivia events are to deep earthquakes in general. We thus hope to shed some light on the continuing debate regarding the physical mechanism of deep events. The method of *Antolik et al.* [1996] is used to invert relative source time functions determined from the deconvolution of body wave phases recorded by broadband stations at teleseismic distances. These time functions, or moment rate functions (MRFs), are mapped onto the spatial and temporal distribution of slip for each event, and the best estimate of the rupture velocity and choice of fault plane is determined from objective analysis of the variance. We compare locations of the moment release to that of the cold slab core using locations of background seismicity and estimate static stress drops for the events using the long period moment and fault dimensions. After a brief review of the method and before describing the application to real data, we carry out several tests of the method on synthetic data and determine its ability to obtain details of the rupture process under a variety of conditions.

## 2. Determination of Moment Rate Functions

In the frequency domain the far-field wave displacement due to a point source recorded at distance $r$ and azimuth $\phi$ can be represented by

$$U^P(\omega) = \dot{M}(\omega)G^P(\omega, r, \phi)R^P I(\omega) \qquad (1)$$

where $P$ represents the particular phase, $\dot{M}$ is the moment rate function, $G$ is the Green's function or re-

sponse of the medium along the wave path, $R$ is the radiation pattern factor, and $I$ is the instrument response. Thus an estimate of the MRF of an earthquake can be obtained by standard deconvolution of the Green's function (after correcting for the radiation pattern and instrument response) from the displacement record. Estimates of the Green's function can be obtained either through calculation of a synthetic seismogram for an accurate Earth model or through the use of a smaller earthquake located close to the event of interest and having a similar focal mechanism. This latter method is known the empirical Green's function (EGF) method. In this study, Green's functions are obtained using both methods.

For a uni-directional propagating source, (1) must be modified to the following form in order to include directivity effects [*Ben-Menahem and Singh*, 1981]:

$$U^P(\omega) = \omega A \dot{M}(\omega)\frac{\sin X}{X}e^{iX}G^P(\omega, r, \phi)R^P I(\omega) \quad (2)$$

where $A$ is the fault area and $L$ is the rupture propagation length. $X$ is known as the directivity parameter and is given by

$$X = \frac{\omega L}{2}\left[\frac{1}{v} - \frac{\cos\psi}{c}\right] \qquad (3)$$

where $v$ is the rupture velocity, $c$ is the phase velocity, and $\psi$ is the angle between the ray direction and the direction of rupture propagation. Thus the MRF shape is modified by directivity, which suggests the possibility of retrieving an image of the rupture history using estimates of the modified MRF at multiple azimuths. In addition, because of the dependence on take-off angle in (3), the MRF shape is also dependent on the particular phase. The use of multiple phases at a particular station can therefore add additional information. For teleseismic records of deep events such as those studied here, the various body wave phases are well separated and lend themselves to easy windowing and deconvolution. Figure 1 shows an example. Figure 1b shows MRFs estimated independently from the direct $P$ and depth phases ($pP$, $sP$) for the March 9, 1994, Fiji Islands earthquake. The second large subevent has a different time delay for each of the three phases, causing a change in duration of the MRF.

We carried out the deconvolution process in the frequency domain after first windowing the desired phase in the seismogram, integrating to displacement, removing the instrument response, and cosine tapering the records. The record length used is 40-60 s (see Figure 1) depending on the source duration. To reduce high-frequency noise in the MRFs, the standard "water level" method [*Clayton and Wiggins*, 1976] is used. This lessens the effect of holes in the spectra. Further low-pass filtering of the MRFs is sometimes necessary to remove interference from side lobes; the corner frequency used varies between events but is consistent between all stations for each event. We used only the vertical com-
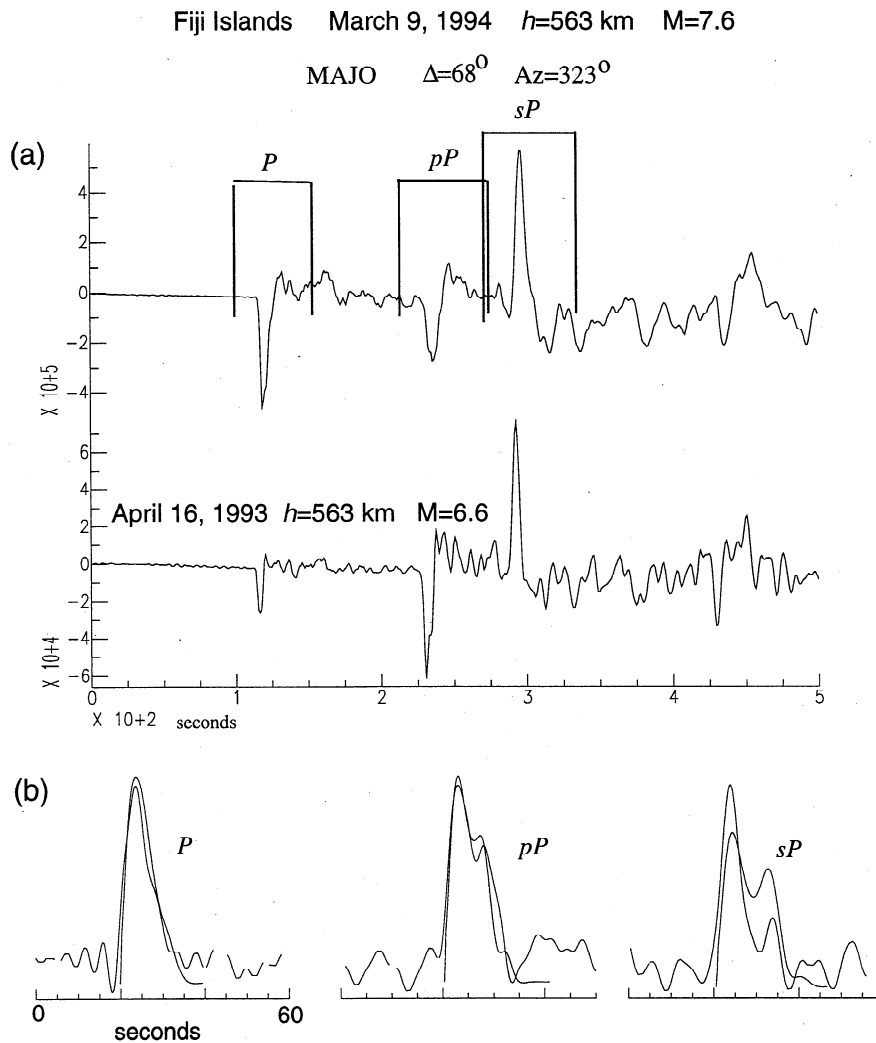
**Figure 1.** Example of deconvolution of body wave phases for the March 9, 1994 Fiji Islands deep earthquake at station MAJO (Matsushiro, Japan). (a) Vertical component displacement seismograms for the mainshock and smaller earthquake used as an empirical Green's function. Time windows for deconvolution are marked. (b) Results of deconvolutions for each of the three phases. Rupture directivity has a differing effect on the moment rate functions (MRFs), as can be seen by the changing time delays of the second subevent. Dashed curves show synthetic MRFs obtained from the inversion method described in this paper [*Antolik*, 1996].

ponents for deconvolution of $P$ phases and either one or both horizontal components for the $S$ waves.

For two of the events discussed in this paper (events 1 and 3, Table 1), EGFs were used either wholly or in part. The major assumption of the EGF method is that the smaller event is essentially a point source in space and time. To the extent that this assumption is violated the MRF of the larger event will be an estimate relative to that of the EGF. There also may be phasing problems resulting from a slightly different focal mechanism or differing location of the EGF (for a discussion of the issues involved in EGF selection and application, see *Velasco et al.* [1994]). At teleseismic distances ($> 20°$) it is usually necessary to use events of $M_w$ 6.0 or larger to achieve adequate signal power. This further restricts the use of the EGF method since it may be difficult to find events satisfying all of the criteria.

The use of synthetic Green's functions eliminates problems reulting from source finiteness. However, in this case one is limited by the accuracy of the Earth model used to calculate them. For this study Green's functions were calculated from a layered parameterization of the IASP91 velocity model [*Kennett and Engdahl*, 1991] using a frequency-wavenumber integration code. Attenuation was incorporated using model QL6 of *Durek and Ekström* [1996].

Because of the simplicity of teleseismic recordings of deep events (deriving largely from the fact that the direct phases have traversed the upper mantle only once from source to receiver), some studies of the deep earthquake source process have assumed that the Green's function is essentially a delta function and that the displacement recordings therefore represent the true source time function. However, we have not used that assump-

**Table 1.** Locations, Focal Mechanisms, and Magnitudes for Events in This Study

| Event[a] | Date (UTC) | Latitude | Lon. | Depth (km) | $M_w$ | $M_o$ (N-m) | Strike 1/Dip 1/Rake 1 ($^\circ$) | Strike 2/Dip 2/Rake 2 ($^\circ$) |
|---|---|---|---|---|---|---|---|---|
| 1 | 940110 | 13.34$^\circ$ S | 69.45$^\circ$ W | 596 | 7.0 | 2.3 x 10$^{19}$ | 238/18/-127 | 96/76/-79 |
| 2 | 940721 | 42.34$^\circ$ N | 132.87$^\circ$ E | 471 | 7.3 | 9.7 x 10$^{19}$ | 60/32/174 | 154/87/58 |
| 3 | 950823 | 18.86$^\circ$ N | 145.22$^\circ$ E | 595 | 7.0 | 4.2 x 10$^{19}$ | 134/43/-117 | 349/52/-67 |
| 4 | 960617 | 7.14$^\circ$ S | 122.59$^\circ$ E | 587 | 7.9 | 7.9 x 10$^{20}$ | 223/51/-131 | 97/54/-51 |
| 5 | 960805 | 20.69$^\circ$ S | 178.31$^\circ$ W | 550 | 7.3 | 1.3 x 10$^{20}$ | 217/20/-95 | 42/70/-88 |

Epicentral information is taken from the NEIC. Focal mechanisms and magnitude information are from Harvard.
[a]The events are numbered in the order they are presented in the text.

tion here, even though the process of deconvolution results in some loss of high-frequency details of the rupture. There are several reasons for this. First, lateral heterogeneity near the source, due to the presence of high-velocity slabs, may still affect the waveforms [*Vidale and Garcia-Gonzalez*, 1988]. Second, the resolving power of the data sets is restricted by less than an ideal azimuthal distribution of stations [*Saraó et al.*, 1998], particularly for events in the southern hemisphere. In addition, the assumptions used to stabilize the inversion process, such as a regular rupture front, and the necessity of dividing the fault into finite cells place into question the ability to recover high-frequency details. Departures from these assumptions are to be expected for large earthquake ruptures, introducing error and nonuniqueness into the solution. We therefore restrict ourselves to only the most resolvable features, such as the location and relative strengths of major subevents. Inversion of MRFs instead of the displacement waveforms also removes the necessity of computing Green's functions during the inversion and therefore reduces the necessary computational resources.

## 3. Inversion of Moment Rate Functions

Our finite fault inversion method is based on that introduced by *Mori and Hartzell* [1990] and extended to regional distances by *Dreger* [1994]. The source parameterization is that of a radially expanding rupture front with the moment release confined to one of the nodal planes as determined by the Harvard Centroid Moment Tensor (CMT) solution. The fit to each observed MRF is obtained by summing synthetics positioned along the fault at equal intervals and taking into account the timing delay due to rupture and wave propagation with respect to the hypocenter. Travel time for each phase used in the inversion is calculated from the IASP91 velocity model. The contribution to the synthetic time functions from each fault cell is a boxcar with a duration that is fixed in each inversion.

The observed MRFs are related to the matrix of synthetic time functions (**B**) by the vector of slip weights **x** on the fault, and we solve a system of equations of

the form

$$\begin{bmatrix} \mathbf{B} \\ \lambda \mathbf{S} \end{bmatrix} \mathbf{x} = \begin{bmatrix} \mathbf{d} \\ 0 \end{bmatrix} \quad (4)$$

where **d** is the vector of observed MRFs. The lower portion of (4) is a spatial derivative minimization constraint designed to smooth the resulting slip distribution (**S** is the matrix of first partial derivatives, $\lambda$ a constant). The slip weight vector is then obtained by standard least squares. Prior to inversion the data are normalized to unit area. In other words, each MRF is assumed to integrate to the long-period scalar seismic moment, and the inversion fits the MRF shape only. From the slip weight vector we determine the value of slip on each fault cell by using an independent seismic moment estimate. The slip amplitudes are thus subject to the same uncertainty normally found in seismic moment estimates ($\pm50\%$).

Other constraints imposed on the inversion include slip positivity and a constant rupture velocity. The importance of using the positivity constraint in order to obtain satisfactory results in inversions of this type has been emphasized by *Das and Suhadolc* [1996]. Each fault cell is allowed to slip only once. The best values of the average rupture velocity and the dislocation rise time (represented by the width of the boxcar functions) are determined by repeated inversions and a standard grid search. In many cases a clear minimum in variance can be obtained by varying the rupture velocity, usually dependent on the slip distribution and the station coverage. The goodness of fit is evaluated by minimizing the variance function given by

$$\sigma^2 = (\mathbf{Bx} - \mathbf{d})^2 / N \quad (5)$$

$N$ is the number of degrees of freedom in the slip model, which varies between inversions according to the number of subfaults contributing to the solution. It is important to take into account the number of free parameters since data can often be more easily fit at higher, unrealistic rupture velocities since a higher rupture velocity usually results in a larger slip model [*Mori and Hartzell*, 1990].
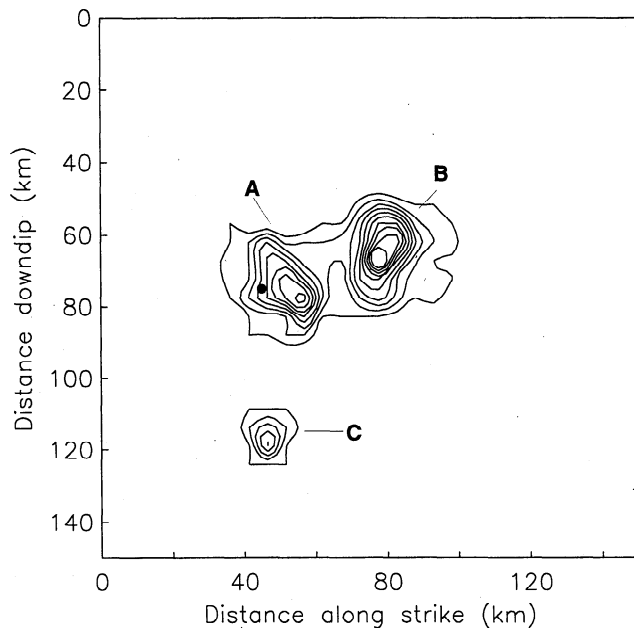
**Figure 2.** Input slip model used for the synthetic inversion tests. The contour level is set at 1/12 of the peak slip and is the same for all subsequent figures. Letters refer to subevents discussed in the text. The dot indicates the hypocenter location.

This method of determining slip history from MRFs differs from other methods such as the radon transform [*Ruff*, 1984; *Hartog and Schwartz*, 1996], that consider directivity in only one direction. Here the slip is allowed to map onto any part of the fault plane as dictated by the data. As stated above, the inversion of MRFs is simple to implement since Green's functions need not be computed in the inversion. As in waveform inversions, the inclusion of data from $S$ waves and depth phases often helps to better constrain the source parameters. This is evident from (3), where the lower phase velocity

for $S$ waves results in directivity having a larger effect on the MRFs than for $P$ waves. A drawback to this method is that changes in directivity along the fault, rupture velocity, or focal mechanism cannot be modeled directly and can introduce error into the solution. This is sometimes a problem for large earthquakes. Some of these issues are investigated in the following section.

## 4. Synthetic Inversion Tests

A number of tests were performed on synthetic data to assess the ability of this simple method to determine accurate slip distributions, rupture velocity estimates, and choice of fault plane under certain conditions. Variations of the input model shown in Figure 2 were used in all cases. The situation is patterned after the March 9, 1994, Fiji Islands deep earthquake and is similar to many of the real cases described below, with one possible fault plane having a steep dip and the other being nearly horizontal. The conditions governing each test case are listed in Table 2 as well as described below.

### 4.1. Uneven Station Distribution

The first inversion test considered the effect of a station distribution that is highly asymmetrical in azimuthal distribution. Synthetic MRFs for a rupture along a near-vertical fault plane (strike 10°, dip 80°) were computed using the slip model of Figure 2 for the irregular distribution of stations shown in Figure 3a. This station distribution primarily covers only a 180° spread in azimuth, and only two stations are located to the east. All phases are $P$ waves. The rupture proceeded horizontally along strike with a third compact subevent located directly downdip from the hypocenter (subevent C). The correct fault plane should be relatively difficult to resolve since the rupture is directed primarily along the common axis of the two possible fault planes (the conjugate "subhorizontal" plane has a

**Table 2.** Summary of Synthetic Test Cases

| Test Case | Station Distribution[a] | Phases | Source Description | Figure[b] |
|-----------|-------------------------|--------|--------------------|-----------|
| 1a | U | $P$ | normal | 3,4 |
| 1b | B | $P$ | normal | 3,4 |
| 2a | U | $P$ | Rupture velocity 3.2 km s$^{-1}$ for subevent B | 5,6 |
| 2b | U | $P$ | same as 2a, with line source for subevent B | 5,6 |
| 3a | U | $P$ | same as 2b, with strike of subevent B focal mechanism 350° | 7,8 |
| 3b | U | $P, S, pP$ | same as 3a | 7,8 |

The "normal" source type is the input model shown in Figure 2, with a circular rupture front, constant rupture velocity (4.0 km s$^{-1}$), and constant focal mechanism (strike 10°; dip 80°) for all parts of the rupture used in the forward problem.

[a]U refers to the uneven station distribution shown in Figure 3a. B refers to the azimuthally balanced station set shown in Figure 3c.

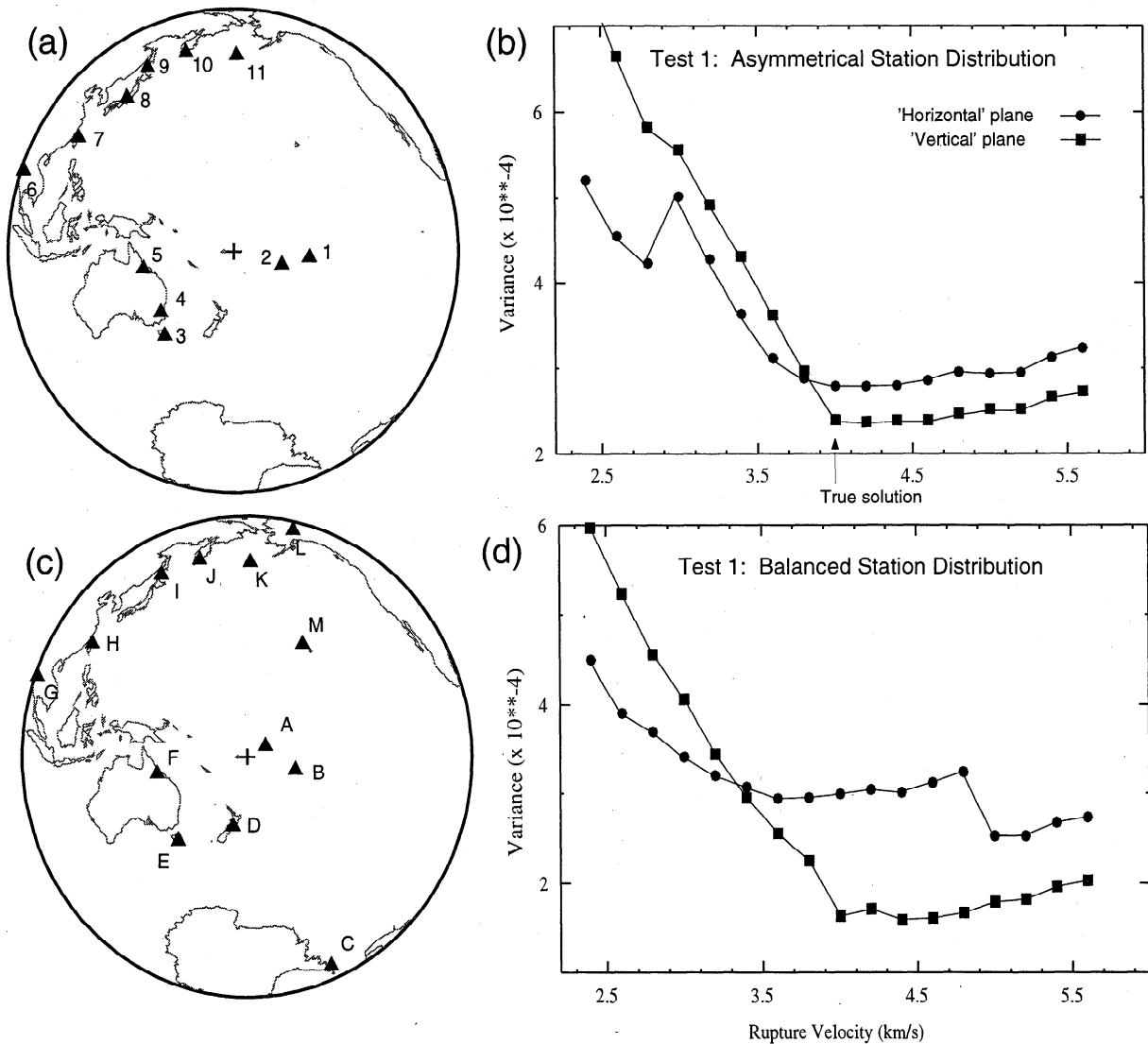[b]Figures in which the results are presented.

**Figure 3.** (a),(c) Distribution of receivers for the inversions in test case 1. Figure 3a shows uneven distribution of 11 stations used for case 1a (Table 2), while Figure 3c shows the symmetrical station distribution used in case 1b. The hypocenter location in each map is the same and is indicated by the cross. (b),(d) Curves of variance plotted vs. assumed rupture velocity for test case 1. The solution for the near-vertical plane is indicated by squares and for the subhorizontal plane by circles. The station distribution for each inversion is indicated by the corresponding left-hand side map. The input model was along the near-vertical plane with a rupture velocity of 4.0 km s$^{-1}$ (arrow). Resolution of the correct fault plane is much improved for the bottom case.

dip of 25$^o$). The input rupture velocity was 4.0 km s$^{-1}$, and a relatively large value of the smoothing parameter (0.5) was used. The fault was divided into 30 cells along strike and 30 downdip.

Results from the inversion are shown in the upper right of Figures 3b and 4b. The correct fault plane is determined very well (variance difference is ∼25%), and the variance increases very rapidly at values of the rupture velocity less than the true value. At higher rupture velocities the inversion is able to find slip distributions that match the data almost as well, emphasizing the importance of considering the number of free parameters. The output slip model is somewhat larger than the

input model, and the amplitude of subevent B is significantly underestimated. In particular, the edges of the rupture are smoothed considerably with false slip produced between subevents B and C. This is caused mainly by the derivative minimization constraint imposed. Another factor is the circular rupture parameterization. This is because at any point in time slip may be occurring anywhere along the locus of a circle with the radius determined by the rupture velocity. The source dimensions are not large enough to determine the exact distribution of slip along this circle from the available data. Subevent C cannot be resolved with this station distribution.
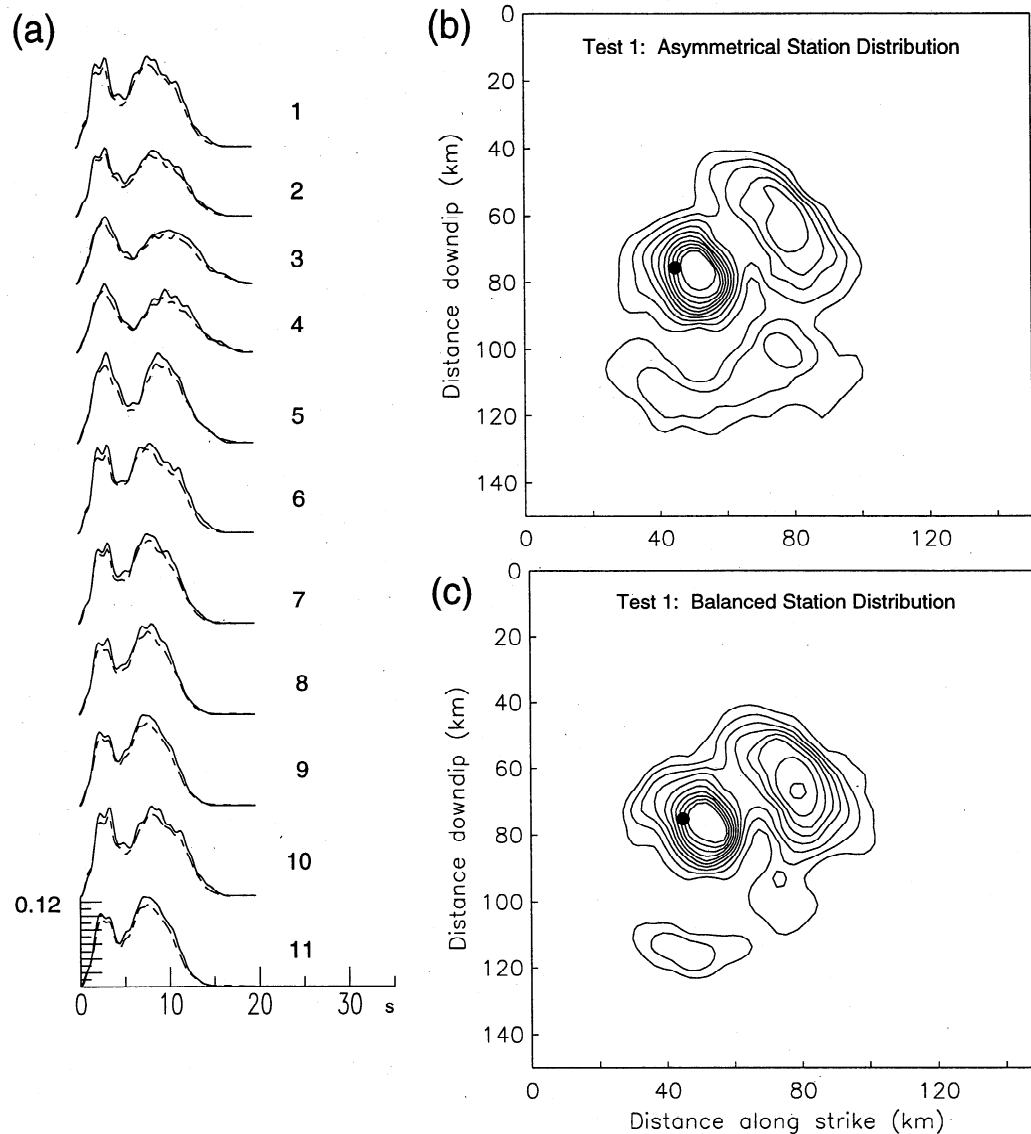
**(a)**

**(b)**

**(c)**



**Figure 4.** Inversion results for test case 1: (a) Input (solid) and ouput (dashed) MRFs are shown for case 1a. (b),(c) Output slip models along the near-vertical plane with a rupture velocity of 4.0 km s$^{-1}$ for the test cases 1a (Figure 4b) and 1b (Figure 4c). Contour level is the same as used for Figure 1. Numbers refer to stations shown in Figure 3. The MRF amplitudes (units of $M_o$ s$^{-1}$) reflect normalization to unit area.

The synthetic MRFs are reproduced almost exactly and are shown for reference in Figure 4. The variance reduction is 99%.

The same inversion was then repeated (case 1b, Table 2) using a much better azimuthally-distributed station set (Figures 3d and 4c). The amplitude of subevent B, about equal to that of subevent A in the input model, is much better recovered. In addition, there is less smearing of the slip and even some indication that subevent C is beginning to become resolved. The variance separation between the fault planes is increased (Figure 3). Otherwise, the position of subevents remains the same. It is therefore concluded that azimuthal station coverage has a significant bearing on the ability to de-

termine relative amplitudes of subevents but that the gross distribution of slip can be recovered with only a 180° azimuthal distribution of data.

### 4.2. Change in Rupture Velocity and Directivity

Next we investigated the effect of a large change in rupture velocity and directivity along the fault plane (test case 2). We mean by "change in directivity" a change in the configuration of the rupture front during the rupture propagation. The rupture velocity for subevent B was decreased to 3.2 km s$^{-1}$ when computing the synthetic data, and the inversion was carried out
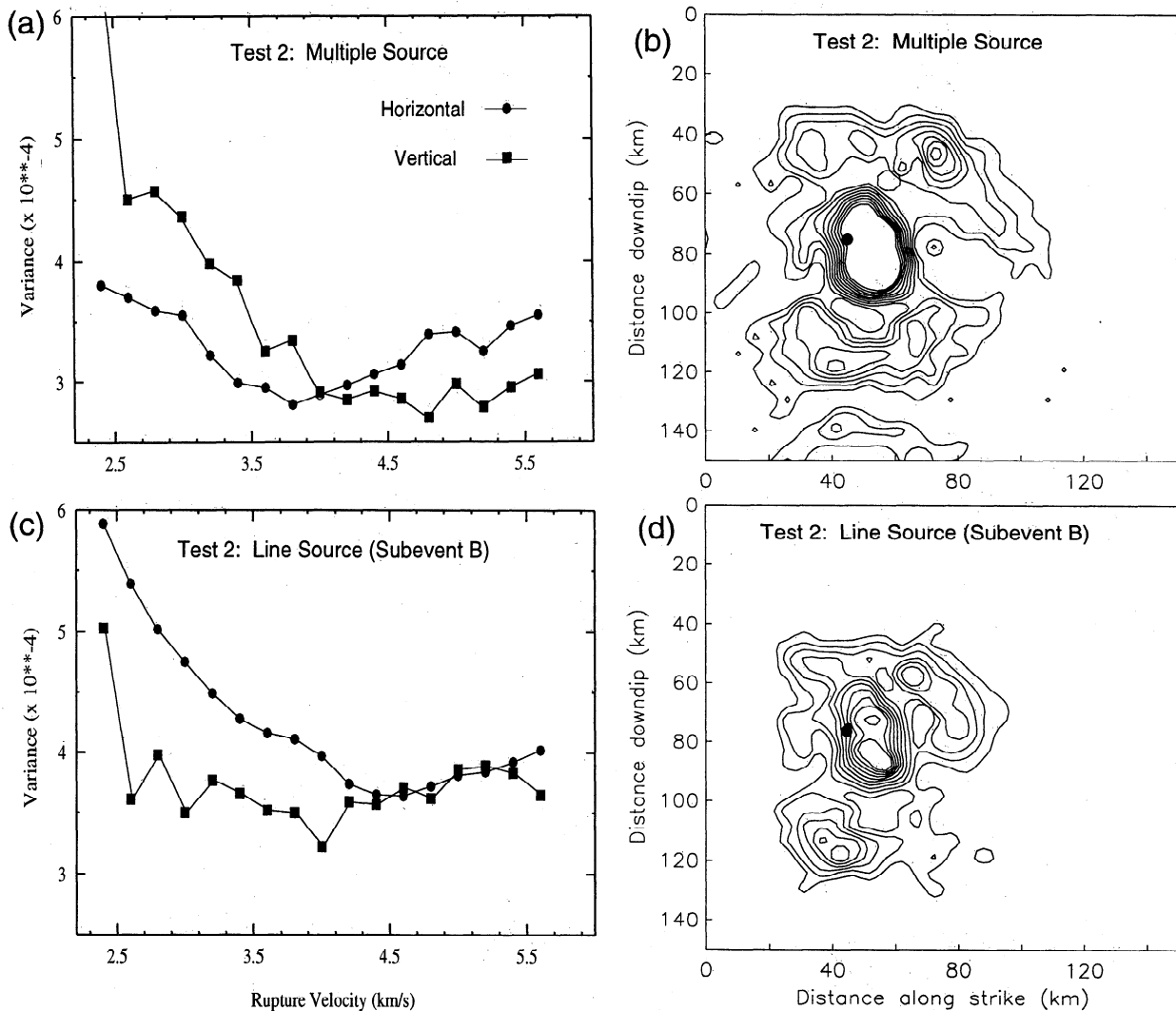
**Figure 5.** Results are shown for inversion test 2. Variance curves are shown for cases (a) 2a and (c) 2b. See the text and Table 2 for details. Symbols are the same as in Figure 3. Output slip models along the vertical plane (rupture velocity 4.0 km s$^{-1}$) are shown for cases (b) 2a and (d) 2b. The contour level is again the same as used for Figure 1.

using the asymmetrical station distribution from test 1. Subevent B was treated as an independent event, with the slip also beginning at a single point. The rupture in effect consisted of a multiple source. In addition, random noise was added to each synthetic MRF with a maximum amplitude of 10% of the peak. These results are shown in Figures 5a and 5b.

Under these conditions it is seen that the correct fault plane cannot be determined. The abrupt change in rupture velocity also cannot be resolved, although this is perhaps to be expected since most of the rupture still propagates at 4.0 km s$^{-1}$. The rupture velocity giving the lowest variance is 3.8 km s$^{-1}$ for the subhorizontal plane and 4.8 for the vertical. However as before the variance curve is flat above 4.0 km s$^{-1}$.

The directivity change has a large effect on the synthetic MRFs as can be seen in Figure 6a. The variation in width of the MRFs is reduced, and the duration of

the second pulse is greatly increased. This is probably the reason for the lack of sensitivity to the fault plane. The multiple-source parameterization introduces a large component of vertical directivity into subevent B. As a result, the output model has shifted its location upward on the fault plane (Figure 5b) in an effort to fit the data under the constraint of a radially expanding rupture.

This inversion was also repeated (case 2b, Table 2) using a propagating line source as the rupture parameterization for subevent B (lying within the two-dimensional rupture plane) in computing the synthetic data in order to better approximate a radially expanding rupture. The inversion retained the original regular rupture parameterization. Thus the synthetic MRFs shown in Figure 6b are very similar to those in Figure 3. As a result, the locations of subevents are better recovered, including that of subevent C. There is also better resolution of the fault plane (below 4.2 km s$^{-1}$ the difference is sig-

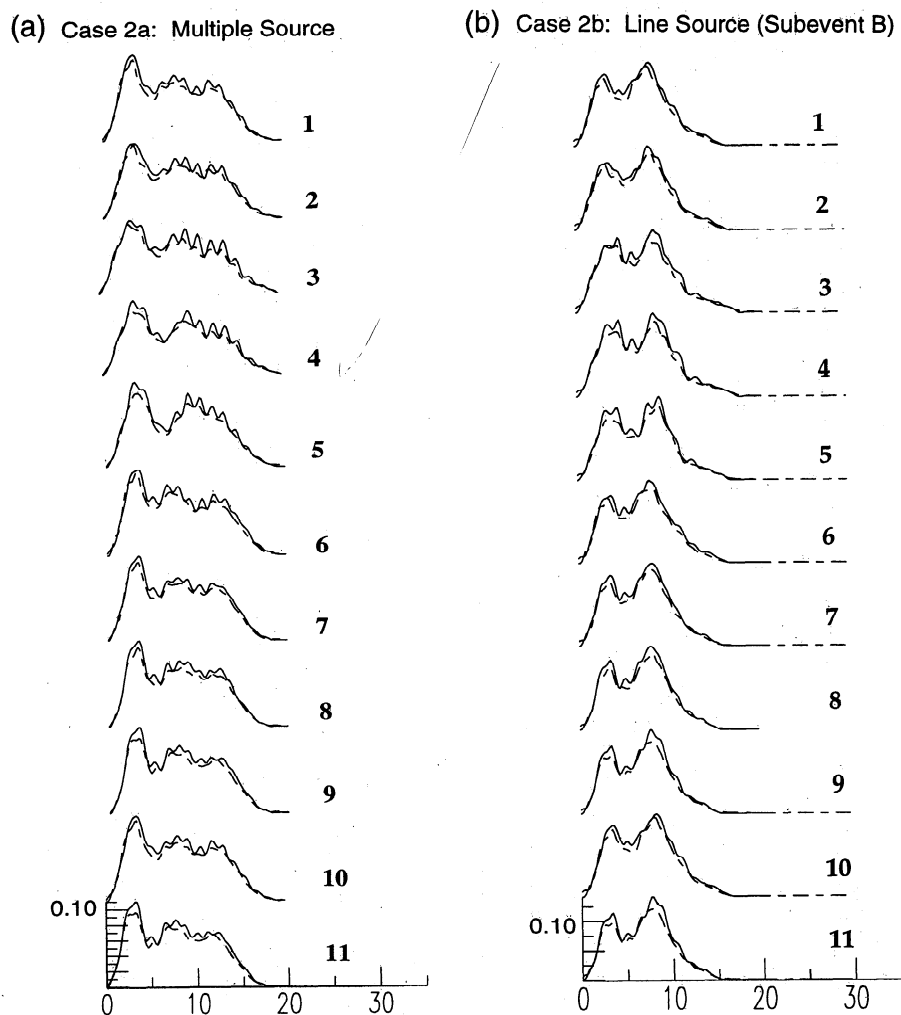**(a)** Case 2a: Multiple Source    **(b)** Case 2b: Line Source (Subevent B)



**Figure 6.** Input (solid) and output (dashed) MRFs are shown for test case 2: (a) the circular rupture parameterization in the forward problem for subevent B (case 2a), and (b) the line-source representation (case 2b). Numbered stations are the same as for the MRFs plotted in Figure 4. The effect of random noise added to the MRFs can be seen for case 2a.

nificant). Although the smallest variance still occurs at 4.0 km s$^{-1}$, the curve for the near-vertical fault plane is essentially flat down to 2.6 km s$^{-1}$. It is apparent that directivity changes during rupture can result in false shifts in the locations of subevents and can also affect the ability to distinguish between the fault and auxiliary plane. However this is probably only a significant factor for the largest event considered, the Flores Sea earthquake (and also for the Bolivia earthquake considered by *Antolik et al.*, 1996).

### 4.3. Change in Focal Mechanism

For this test (test case 3), synthetic seismograms were computed for an input model where subevent B was given a rotation in strike from 10° to 350°. Its rupture velocity remained at 3.2 km s$^{-1}$. The focal mechanism of the rest of the model remained as before. Point source synthetic seismograms were deconvolved from the first set of seismograms to produce synthetic MRF

data, which were then inverted along the original nodal planes. Thus this test also differs from the two previous tests in that it includes the effects of noise resulting from the deconvolution process and from a differing position along the fault of the EGF. Two data sets were tried, first P waves from the original 11 stations (case 3a) followed by a set of 22 total waveforms (11 P, 7 S, 4 pP) from the same 11 stations (case 3b). Results are shown in Figures 7 and 8.

Under these extreme test conditions, neither the actual fault plane nor the details of the slip distribution can be recovered well. However, the near-vertical plane still gives a smaller variance throughout. The difference is only slightly better than 5% for the first data set and marginally improved for the second, which would not be considered significant (level of significance <50% from an F test). Subevent B is also moved downward on the fault plane. Both the amplitude and position of subevent B are improved with the addition of the S
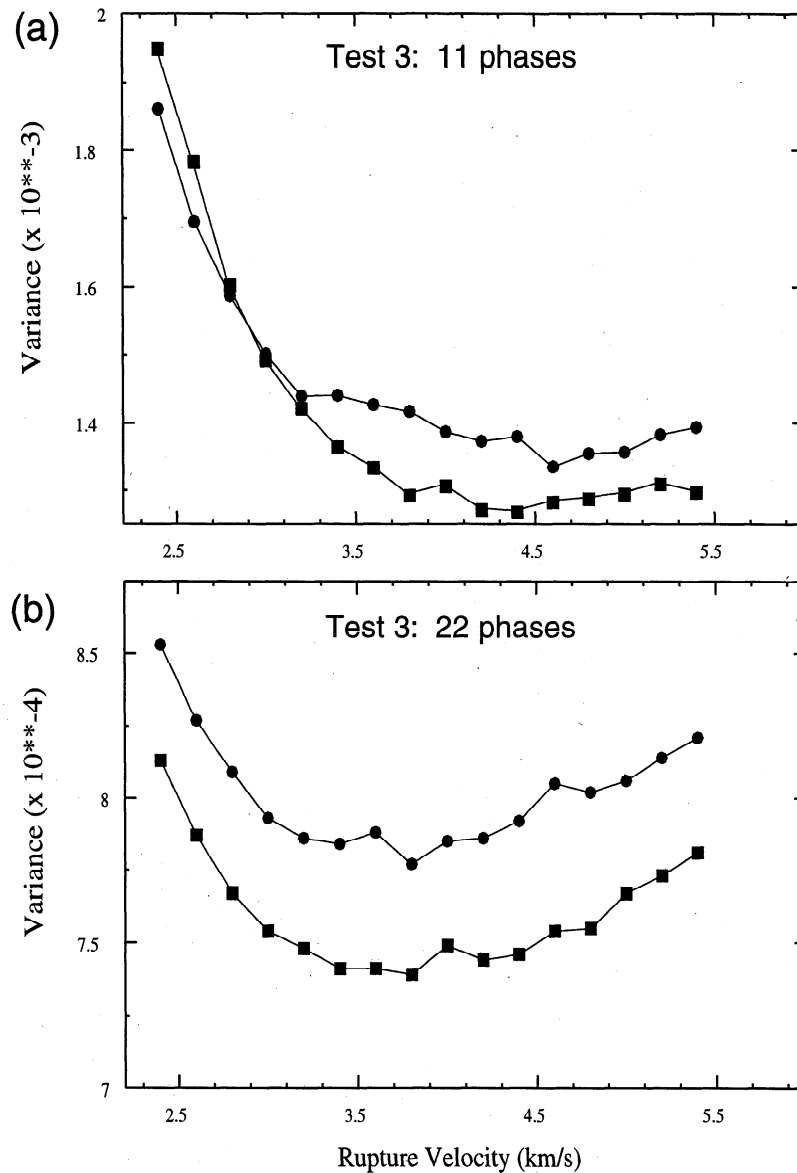
**Figure 7.** Variance curves for inversions in test case 3 which invlove a differing focal mechanism for subevent B in the forward problem: (a) inversions involving only $P$ waves from the original set of 11 unevenly distributed stations (case 3a) and (b) inversions involving a combination of 22 $P$, $S$, and $pP$ phases from the same set of stations (case 3b).

waves and depth phases. This illustrates the constraint on vertical directivity provided by the inclusion of depth phases since for a fault plane which is close to vertical, little resolution can be provided on the vertical extent of rupture using strictly downgoing phases. As can be seen from Figure 8, the shape of the MRFs is affected by the focal mechanism change. Despite this fact the data can be reasonably well fit using this simple source parameterization, although as a result, additional error is introduced into the solution.

### 4.4. Summary of Synthetic Tests

The results of these tests indicate a number of ways in which various complicating factors can affect the ability of this method to recover accurately details of the rupture process. In the ideal case (one in which data are available from a set of stations with nearly complete sampling of the azimuthal range, and where the average rupture velocity and slip duration on all portions of the fault are known a priori) we have found that the causative fault plane can be easily distinguished and the pattern of slip well recovered. This is true even when the rupture is directed along the null axis of the two nodal planes. However, the derivative smoothing constraint results in some loss of detail, particularly in low slip areas. This leads to some overestimation of the size of the rupture as well as smearing and dilution of large asperities. Unfortunately, this or similar constraints are usually necessary to stabilize the solution in applications to real data [*Hartzell et al.*, 1991; *Das and*
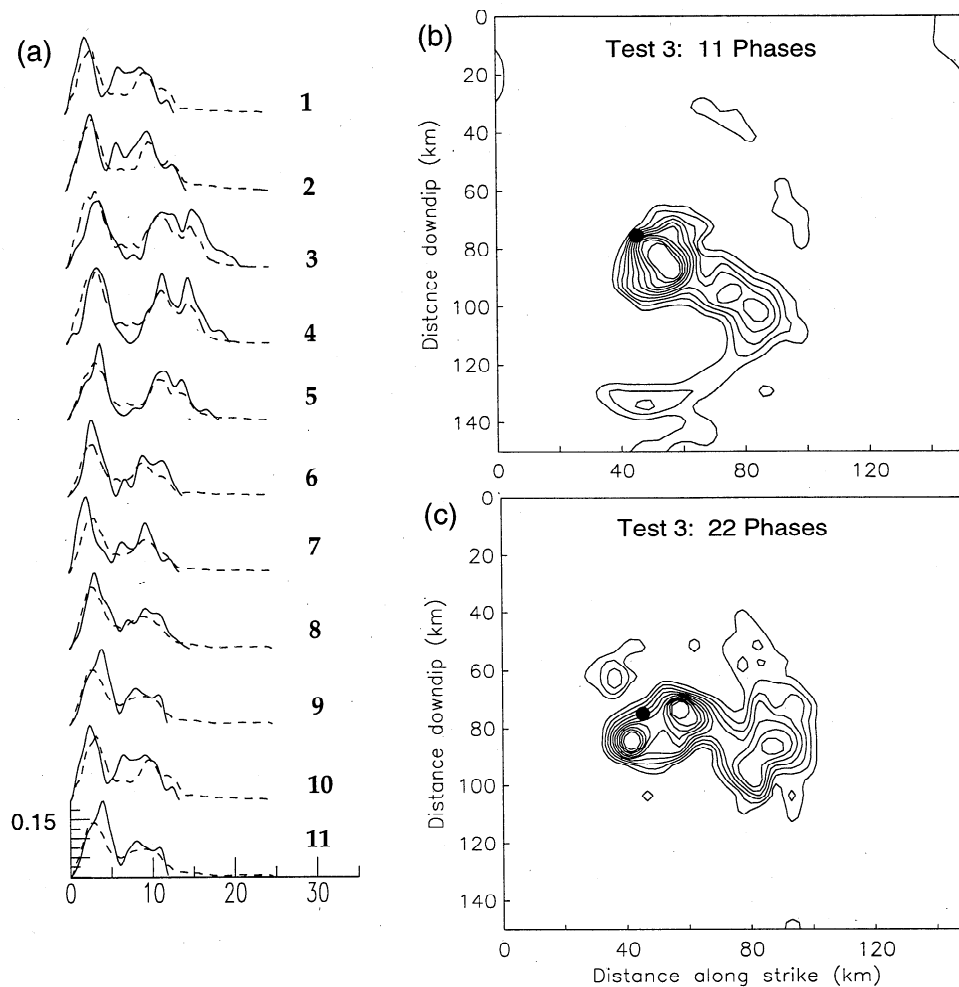
**Figure 8.** (a) Input and output MRFs for case 3a. The change in focal mechanism for subevent B changes the shape of the later portion of the MRFs. The line-source parameterization was used for subevent B when computing the synthetic data. Ouput slip models along the near-vertical plane are shown for cases (b) 3a and (c) 3b.

*Suhadolc*, 1996]. Prescribing a constant rupture velocity (and requiring that each fault cell slip only once) is another method by which we reduce nonuniqueness; this results in the creation of low-level slip artifacts around the border of the rupture, and care must be taken in the interpretation of features which contribute to the later portions of MRFs.

Finally, we have seen that it is not possible to determine the causative fault plane in cases where there are large changes in rupture velocity, focal mechanism, or the timing of moment release along the arcs swept out by the rupture front (cases 2 and 3) when the rupture is directed along the null axis. However, it is worth pointing out that we are not led to the erroneous choice of fault plane in these cases but rather that the two solutions cannot be distinguished. These situations also lead to significant shifts in the locations of subevents and their relative amplitudes, and only the direction of directivity and overall dimensions of the rupture may be discernible. Although use of depth phases and multiple reflections in addition to direct phases may increase the

resolving power of the method, the improvement may be small if all three of the above factors are present.

## 5. Results

### 5.1. January 10, 1994, Peru-Bolivia Earthquake

Complementing our earlier study of the 1994 Bolivia earthquake [*Antolik et al.*, 1996], we applied the above described procedure to teleseismic body wave recordings of the large foreshock which we previously used as an EGF for the mainshock. This event, occurring 5 months previously, was located about 200 km west of the mainshock (Figure 9). Deconvolutions were carried out using theoretical Green's functions and also the largest aftershock of the Bolivia sequence, a $M_w$ 5.5 event occurring on August 8, as an EGF for some of the closer stations (SJG-San Juan, Puerto Rico, LPAZ-La Paz, Bolivia, PPT-Papeete, Tahiti). Use of the EGF permitted the inclusion of the regional station LPAZ. Examples of MRFs for a number of $P$ and $SH$ phases
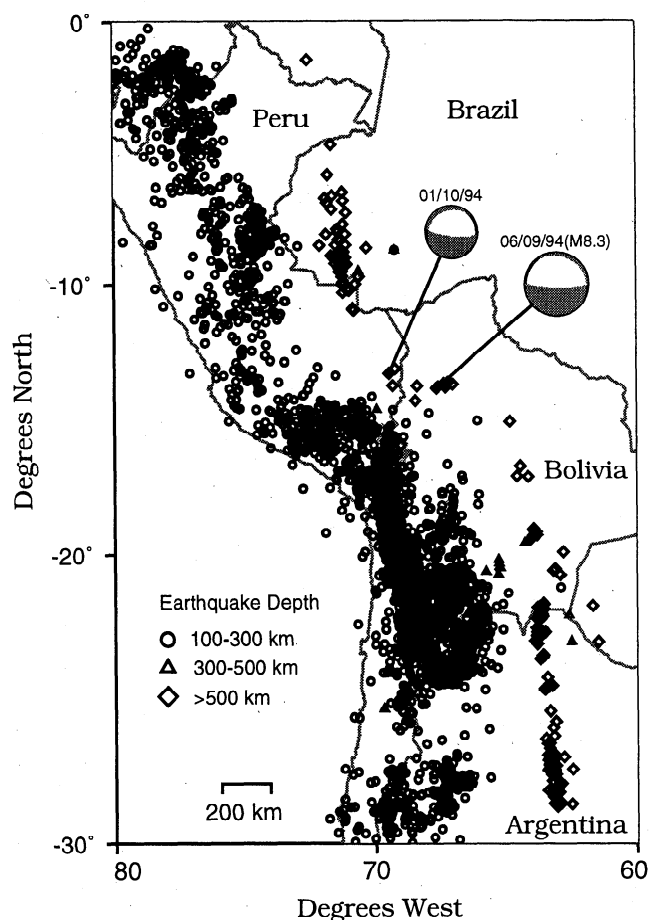
**Figure 9.** Map showing intermediate and deep seismicity of central South America and the locations and focal mechanism of the January 10, 1994 earthquake. Different symbols refer to earhthquakes in different depth ranges. The June 9, 1994 great Bolivian mainshock ($M_w$ 8.3) is also shown. All earthquake locations are from the National Earthquake Information Center (NEIC), and focal mechanisms are from Harvard.

Both fault models give a similar slip distribution showing directivity toward the west. If the horizontal plane is the fault plane, then the details of the slip are very similar to the June 9 mainshock with the individual subevents showing northward directivity. It is possible that a gap in slip between the subevents, such as that seen between the initiation and main moment release for the mainshock, exists here but cannot be resolved because of the small source dimensions. Overall, the similarity in slip distribution is strongly suggestive of a similar physical rupture mechanism. Rupture dimensions for the best model are roughly 20 x 20 km².

Assessment of the relationship of the moment release to the slab core or a wedge of metastable olivine is difficult owing to the almost total lack of seismicity in the immediate surrounding area. The nearest earthquake deeper than 500 km of significant size occurring within the last 35 years is the August 15, 1963 shock of $M$ $7\frac{3}{4}$ that is listed at a depth of 543 km. Only one other event is located nearer than 50 km, and the main Bolivia sequence of June 1994 occurred between 150 and 300 km to the east. However, the location of this earthquake and the elongate E-W distributed pattern of moment release are consistent with the strike of the deep slab as defined by the June 1994 sequence. The majority of the moment release in the June 9 mainshock also lies along an E-W axis [*Antolik et al.*, 1996; *Ihmlé*, 1998]. *Myers et al.* [1995] report that the aftershock sequence for the June 9 event occurred primarily deeper than and northeast of the hypocenter. The aftershocks define a slab having a strike of N68W and dipping 45° toward the northeast. The thickness defined by the hypocenters is ~30 km. If the slab in the vicinity of the January 10 event has similar or greater thickness, then the ~20-km dimension of the slip perpendicular to the slab strike implies that moment release was contained entirely within the slab core. Since, as is seen in the synthetic tests, slip often dies off gradually with this inversion the width of the rupture may well be no more than 15 km. To connect with the N-S striking zone of deep seismicity in western Brazil (Figure 9), the slab must curve toward the north somewhere to the west of the January 10 earthquake.

Two features of this event differ from those of the mainshock. First, there is no evidence of an abnormally low rupture velocity. Lower values than the minimum (3.0 km s$^{-1}$) give significantly poorer data fits. Variance increases slowly at higher values of the rupture velocity, so that the highest value permitted by the data is much less clearly determined. The variance curves for the two nodal planes cross at 5.0 km s$^{-1}$. This is an artifact caused by concentration of the slip along the edges of the fault grid. The second feature is the low slip values, although they should be interpreted with caution. We obtain a peak value of only 1.0 m. If the source areas of the subevents are extremely small, underestimation of the absolute slip values may result from the inversion spreading moment release to adjacent cells, both
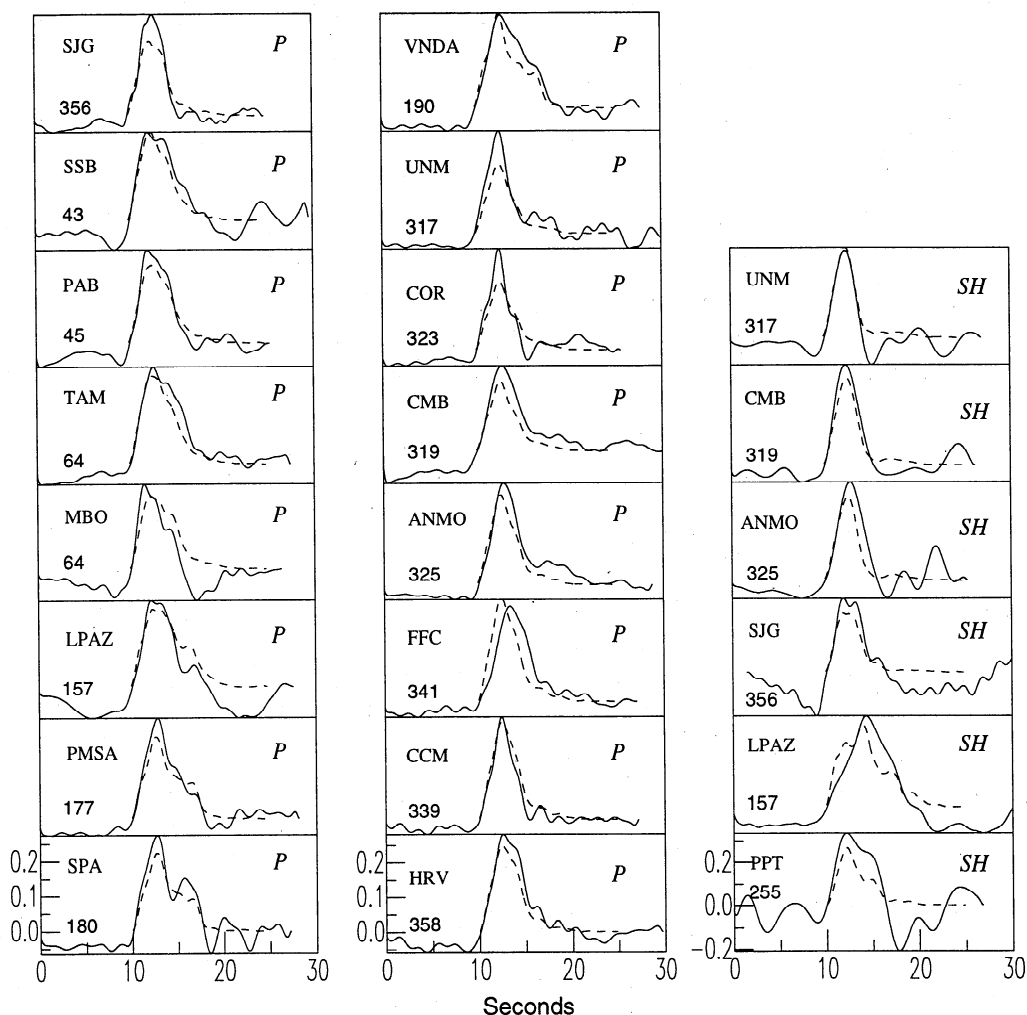
are shown in Figure 10. Most of the MRFs have a simple triangular shape; however, the effects of directivity are clearly evident as stations to the north (e.g., SJG, UNM-Mexico City, COR-Corvallis, Oregon) and west exhibit shorter, simpler pulses than stations at other azimuths and at some southern stations (SPA-South Pole, LPAZ) a second subevent is visible.

For the fault inversion we chose a square grid 40 km on a side and divided into 16 cells along each dimension. As can be seen from Figure 11, confining the slip to the subhorizontal nodal plane (dip of 18°) results in a lower variance for most values of the rupture velocity, although the difference between it and the vertical plane inversion is small. All source studies of the Bolivia mainshock have concluded that the horizontal nodal plane was probably the fault plane. We show in Figure 12 the slip distributions resulting from both inversions. Overall, the fit to the MRFs is excellent, with a variance reduction of 95%.

**Figure 10.** Observed (solid) and synthetic MRFs (dashed) for the best fitting slip model for the January 10, 1994, Peru-Bolivia earthquake. Phase is indicated at the upper right of each panel. Numbers at the bottom left indicate the azimuth of each station from the source. Traces have been low-pass filtered with a corner at 0.5 Hz.

from lack of adequate spatial resolution and use of the smoothing constraint.

To calculate the stress drop, the area of all fault cells exhibiting > 5% of the peak was summed, the result of which was used in the relation [*Kikuchi and Ishida*, 1993]

$$\Delta\sigma = 2.5M_o/A^{1.5} \qquad (6)$$

where the seismic moment is in units of N-m, and $\Delta\sigma$ in Pa. The same procedure was used to calculate source areas and stress drops for all of the events. Using a maximum value of 4.8 km s$^{-1}$ for the rupture velocity from Figure 11 results in a stress drop of 5-15 MPa. This is up to several times smaller than most estimates for the Bolivian mainshock.

## 5.2. July 21, 1994, Japan Sea Earthquake

Like the previous event, the 1994 Japan Sea earthquake ($M_w$ 7.3) also occurred in a complex region

of the deep slab where there is rather sparse background seismicity (Figure 13). The hypocenter is located downdip of the Hokkaido corner between the Kuril and Japan trenches. Focal mechanisms in this area show a widespread departure from down-dip slab compression, particularly at intermediate depths [*Glennon and Chen*, 1993]. Lateral stresses or tearing of the slab have been cited as reasons for this [*Lundgren and Giardini*, 1990; *Zhou*, 1990]. A nearly vertical linear alignment of hypocenters has been identified in the region, although these particular events indicate downdip slab compression [*Lundgren and Giardini*, 1992]. A small subset of events exhibits mechanisms similar to the most recent event, none large enough to be suitable as an EGF. Therefore the deconvolutions of $P$ and $SH$ phases were performed using synthetic Green's functions. The Green's functions were calculated at the same location and depth as the hypocenter.

Figure 14 shows the data set for the inversions, which were carried out on a fault grid having a length of 120
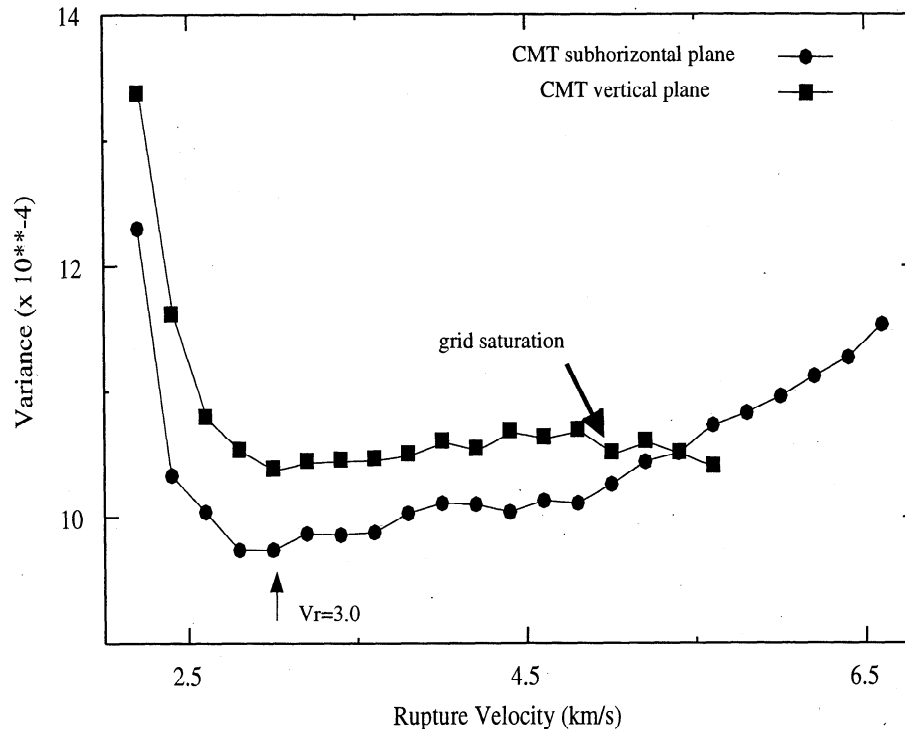
**Figure 11.** Inversion results for the Peru-Bolivia earthquake. The horizontal fault plane gives smaller variance but the difference is not significant. The best rupture velocity is 3.0 km s$^{-1}$. Variance decrease at higher rupture velocities for the vertical plane is caused by saturation of slip on the edges of the fault grid.

km in each dimension and divided into 1600 cells. Two large subevents appear prominent in the MRFs. The first has a large amplitude and short duration at NNE azimuths. However the MRFs have shorter durations overall to the southeast, suggesting strong directivity in this direction. The inversion results are very consistent with these observations.

First, the shallow-dipping nodal plane gives a much smaller variance that is significant at the 95% confidence level and clearly indicates that this plane is the fault plane (Figure 15a). Second, the slip distribution indicates that the first subevent ruptured primarily in a northward direction, while the second large subevent is offset by some 30 km to the SSE of the hypocenter. A large gap in moment release lies between the hypocenter and this subevent. The small peak of slip offset about 20 km to the west has negligible contribution to the calculated MRFs and is not considered reliable. A clear minimum in the variance is obtained with a rupture velocity of 4.6 km s$^{-1}$.

For comparison the slip distribution on the vertical nodal plane is shown in Figure 16. As additional evidence for rupture along the shallow-dipping plane, it is seen that moment release concentrates near the projection of this plane. A similar horizontal distribution of subevents is obtained for the vertical plane. This suggests that the rupture features of this earthquake are well resolved. The level of resolution is probably in-

dicative of the favorable location of the event in an area where excellent azimuthal coverage can be obtained at teleseismic distances.

The small source area for this event leads to a static stress drop estimate in the range 12-30 MPa. Thus it is more similar in this regard to the great Bolivian event. It is noted that the orientation of the subevents resembles the distribution of seismicity in the shallow portion of the Hokkaido corner (Figure 13), which changes in strike from NE to NNW. A tear in the deep slab may exist at this location. If the small western peak of moment release is ignored, the source dimension is only about 10 km perpendicular to the slab strike, which is well within what has been estimated for the thickness of a wedge of metastable olivine at this depth, or from the thickness of a double zone of deep seismicity (15-20 km) at a similar depth in the Izu-Bonin subduction zone [*Kirby et al.*, 1991; *Iidaka and Furukawa*, 1994]. Unfortunately, the sparse background seismicity does not allow delineation of the precise location of the active portion of the slab. We show in Figure 17 a cross section of the nearby seismicity, which shows that the slab dips at a very shallow angle ($\sim$30°). The location of the second subevent plots at or near the bottom boundary of the Wadati-Benioff zone. The rupture may have been stopped by the lower slab edge.

Finally, the results obtained here are similar to those of *Chen et al.* [1996]. They parameterized the rupture
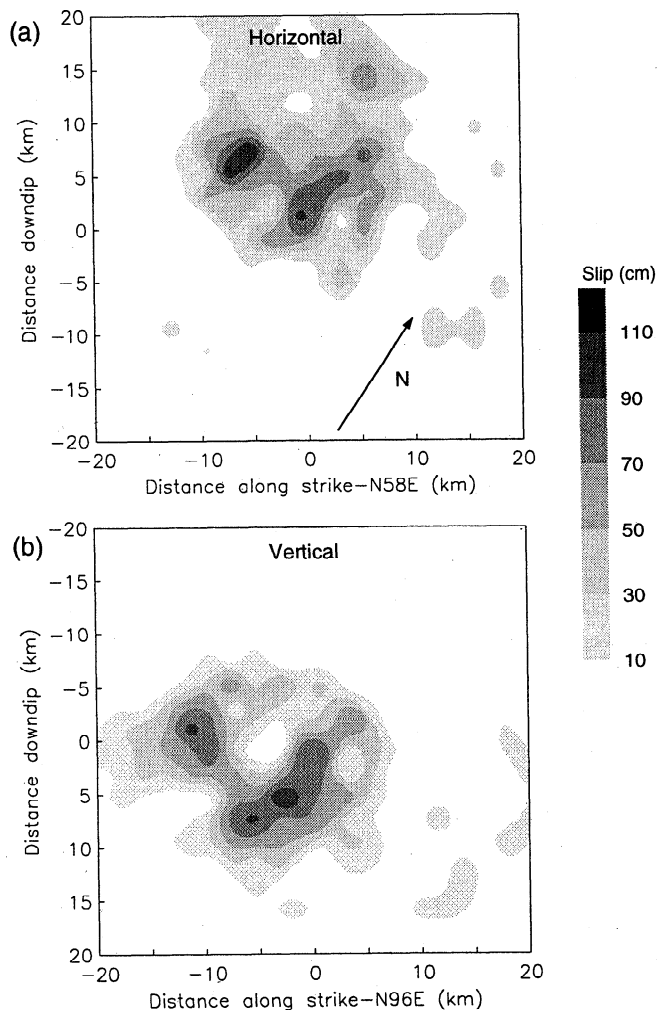
**Figure 12.** Slip models for (a) the subhorizontal fault plane and (b) the vertical fault plane for the Peru-Bolivia earthquake, obtained with a rupture velocity of 3.0 km s$^{-1}$. View is normal to the fault with updip direction toward the top. The hypocenter is located at the origin for each plot. General rupture direction is toward the west for both planes. Details are discussed in the text.

as two subparallel line sources and obtained a separation of ~12 km between the subevents in a SSE azimuth along a shallow-dipping fault plane. Their horizontal separation is roughly half that obtained here; however, they infer a rupture velocity of only 1-2 km s$^{-1}$ between the subevents.

### 5.3. August 23, 1995, Mariana Islands Earthquake

The Marianas slab is one of the oldest portions of subducted lithosphere on Earth and is subducting with a very high velocity. Correspondingly, a rather high rate of seismicity characterizes the deep slab. Unlike the Japan Sea event just discussed, the 1995 Mariana Islands earthquake produced a fairly extensive aftershock sequence [*Wiens et al.*, 1996]. At least three aftershocks

were large enough to be well recorded teleseismically, including a $M_w$ 6.2 shock which occurred 20 hours after the mainshock. This event was found to be suitable for use as an EGF despite the fact that it has a slightly different focal mechanism than the mainshock (Figure 18). The earthquake sequence occurred in a portion of the deep slab where the backround seismicity changes strike locally from north to WNW. The mainshock focal mechanism (indicating normal faulting on two 45°-dipping planes striking to the NW or SE) shows downdip slab compression and is typical of other events in the region. *Lundgren and Giardini* [1992] have found lineations of hypocenters consistent with both of the nodal planes; thus it is not clear which plane is the a priori preferred fault plane. Most of the aftershocks are located along the WNW-striking portion of the slab.

Moment rate functions estimated from $P$ and $S$ phases are shown in Figure 19. Two large subevents are visible with a total source duration of ~6 s. At western azimuths the two subevents merge into a single pulse with very short durations. This indicates strong directivity in this direction. At stations to the north and northeast a third subevent is visible ~7 s after the onset time. This may not be real as discussed below.

Before inversion the MRFs were low-pass filtered with a corner at 1 Hz (as shown in Figure 19). The fault grid consisted of cells with an area of 4 km$^2$. The SW-dipping nodal plane gave a much better solution (40% variance difference) that is significant at the 99% confidence level (Figure 20). The better fit afforded by the SW-dipping plane is easily seen in Figure 19 as the short durations to the west, particularly of the $S$ waves, cannot be fit by the other plane. Westward directivity for the NE-dipping plane would require upward directivity to the rupture and since the rays leave the source downward this rupture geometry lengthens the duration of the MRF by 1-2 s for western azimuths. In addition the large pulse at Guam (GUMO) is very poorly fit by the NE-dipping plane. This observation is crucial because GUMO ($\Delta=5°$) is an upgoing phase. The rupture velocity is not very well constrained as values higher than the shear wave velocity produce significantly better data fits and thus the variance function does not increase significantly despite the greater number of free parameters (Figure 20a). However a velocity less than the shear wave velocity is not inconsistent with the data. There is a significant increase in variance below 3.5 km s$^{-1}$. If the rupture velocity is assumed to be less than the $S$ velocity, then the static stress drop for the event is estimated at 20-48 MPa.

The best-fitting slip model (Figure 20b) consists of two areas of large moment release separated by ~15 km in the downdip direction and to the west. A possible small third subevent is indicated to the northwest. Once again, there is little or no slip between these subevents. The width of the rupture is no more than 15 km perpendicular to the slab strike, and it is totally contained within the zone of background seismicity. It is therefore
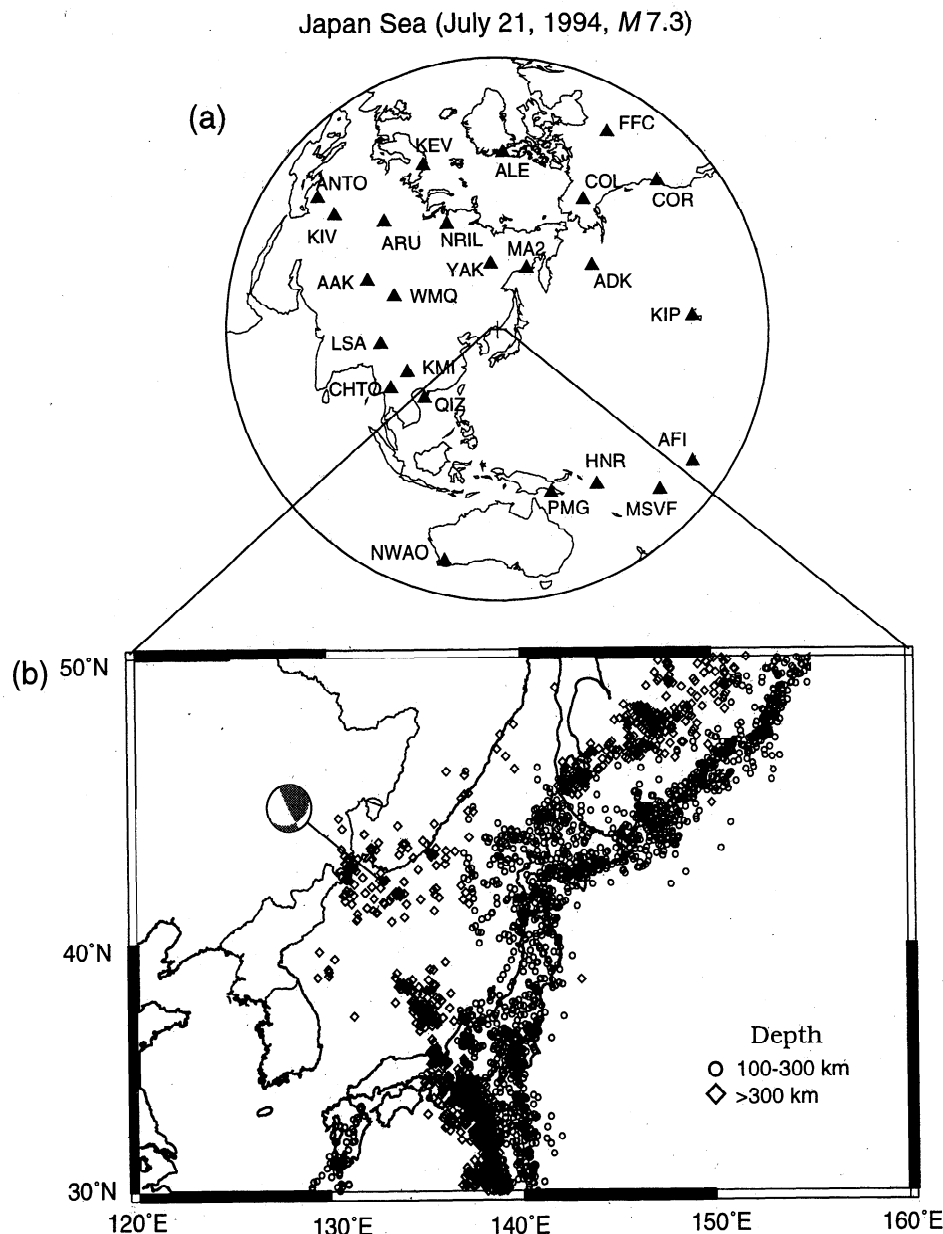
Japan Sea (July 21, 1994, $M$ 7.3)



**Figure 13.** Map of region of the July 21, 1994, Japan Sea earthquake along with intermediate and deep background seismicity. Different symbols indicate different earthquake depth ranges. Figure 13a shows locations of stations used for the source inversion.

likely that the entire moment release occurred within the slab core. A 15 km minimum thickness for the seismically active zone would be similar to that estimated by *Glennon and Chen* [1995] for an event in the Izu-Bonin subduction zone at a depth of 500 km (15-40 km).

Also shown in Figure 20 are the hypocenters of aftershocks occurring within 6 months of the mainshock ($m_b > 4.0$) projected onto the fault plane. Many of these events, including most of those occurring within 2 days, surround the borders of the rupture where the stress concentration would be expected to be highest. This provides additional confidence in the reliability of the slip distribution.

It was noted above that the focal mechanism of the EGF used was slightly different than that of the mainshock (the strike of the SW-dipping plane is rotated counterclockwise by 20°). The inversion was repeated using theoretical Green's functions computed for the mainshock focal mechanism in order to test the effect which this has on the results. As shown in Figure 21, the shapes of some the MRFs are somewhat altered, especially at station GUMO where the synthetic fit is very poor. This is probably the result of an inadequate velocity model since this is a regional station located along the slab strike and the ray paths traverse a large portion of the slab. In addition, for $P$ waves at north and northeast azimuths no evidence, except at one sta-
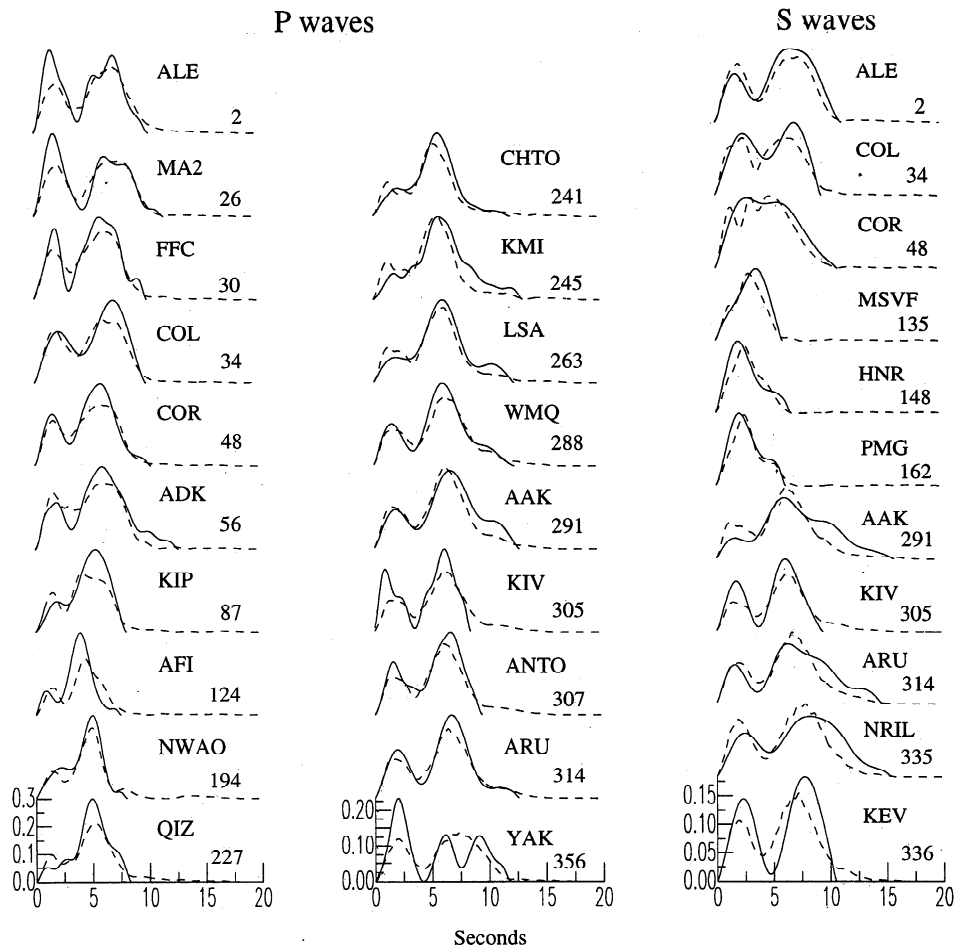
**Figure 14.** Observed (solid) and synthetic (dashed) calculated from the best slip model for the Japan Sea earthquake. The lxeft two columns show MRFs obtained from $P$ waves and the right column from $SH$ waves. The azimuth of each station is indicated to the right. All traces have been low-pass filtered at 0.2 Hz.

tion, is seen for the pulse of moment release following the onset time by 7 s. This suggests that this pulse is caused by a phase which lies near a node in its radiation pattern for this focal geometry and that the slight rotation in mechanism for the EGF causes its contribution to the MRFs to remain after deconvolution. One possibility is a phase converted from an $S$ to a $P$ wave at the 660 km discontinuity ($S660P$), which has approximately the correct timing. In the obtained slip model this pulse is fit by some of the low level patches of slip surrounding the second large subevent. Also, the durations of some of the $S$ wave MRFs are lengthened resulting in further degradation of the data fits. Inversion of the data set in Figure 21 resulted in a slip distribution which contained some differences in the strengths of the subevents from that shown in Figure 20. The data fits, however, were significantly poorer (Figure 21).

Since the Harvard CMT mechanisms are obtained from relatively long period waves, it is certainly possible that a significant portion of the moment release of the main shock occurred with a mechanism more sim-

ilar to the EGF. This could also help explain why the inversion using the EGF gives better results. We repeated the inversion using a plane with a strike of the EGF. Although the variance reduction for this inversion was slightly higher, the overall results were very similar to those shown in Figure 20 and are not shown here.

### 5.4. June 17, 1996, Flores Sea Earthquake

The Flores Sea, Indonesia earthquake ($M_w$ 7.9) is one of the largest deep events in the instrumental catalog. It occurred directly downdip of a kink in the descending slab which is concave toward the backarc side of the trench, opposite in sense to the kink which occurs in the area of both the Japan Sea earthquakes and the 1994 Bolivian event. In this case the bend is caused by impingment of the Australian continental shelf to the east, creating the Timor trough. The convergence direction between the Indo-Australian and Pacific plates is toward the NNE [*DeMets et al.*, 1990]. As Figure 22 shows, this area of the slab contains abundant deep
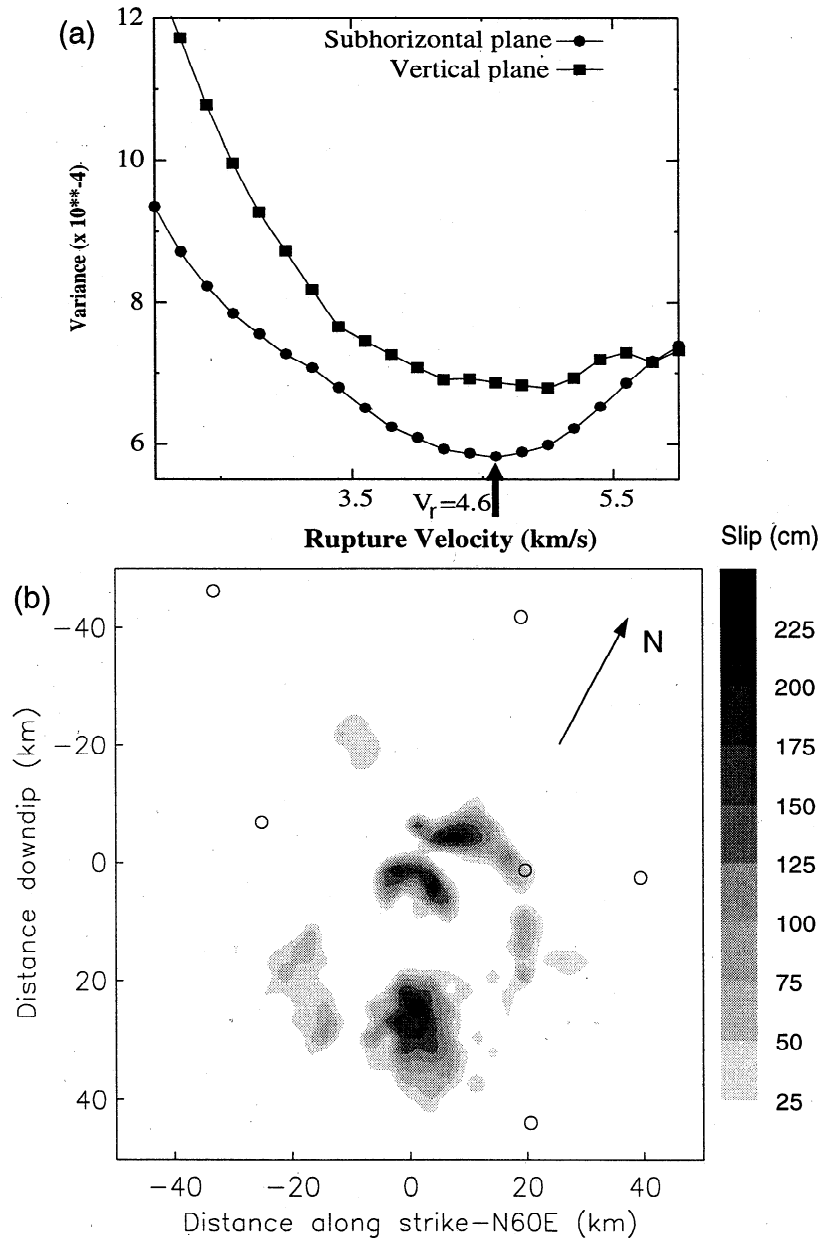
**Figure 15.** (a) Variance curves from fault inversion of the Japan Sea earthquake. Data fits are significantly better for the subhorizontal fault plane and the best rupture velocity is 4.6 km s$^{-1}$. (b) Slip model for the subhorizontal fault plane (rupture velocity 4.6 km s$^{-1}$). View is again normal to the fault with the along strike direction along the positive $r$ axis. Nearby earthquakes deeper than 400 km are shown as the circles.

seismicity with which to compare the location of the moment release. These hypocenters indicate that the active portion of the slab is nearly vertical and has a thickness of ~40 km [*Cardwell and Isacks*, 1978].

The data set of 22 phases shown in Figure 23 was inverted along the two nodal planes of the long period CMT mechanism. This mechanism (Figure 22) indicates left-lateral and normal faulting along one of two moderately dipping planes striking either toward the east or the southwest. The MRFs clearly indicate a complex rupture with a duration on the order of 20 s.

The sharp peak in the time functions at Chiang Mai, Thailand (CHTO) and Xi'an, China (XAN) controls the directivity of the main moment release toward the northwest, although shorter overall durations are observed toward the east. This points to a bilateral rupture.

The fault plane for the inversions contained cells with a dimension of 5 km on a side, and theoretical Green's functions were used for the deconvolutions. Figure 24 indicates that the southward-dipping plane continually gave a better solution, with a higher variance reduction
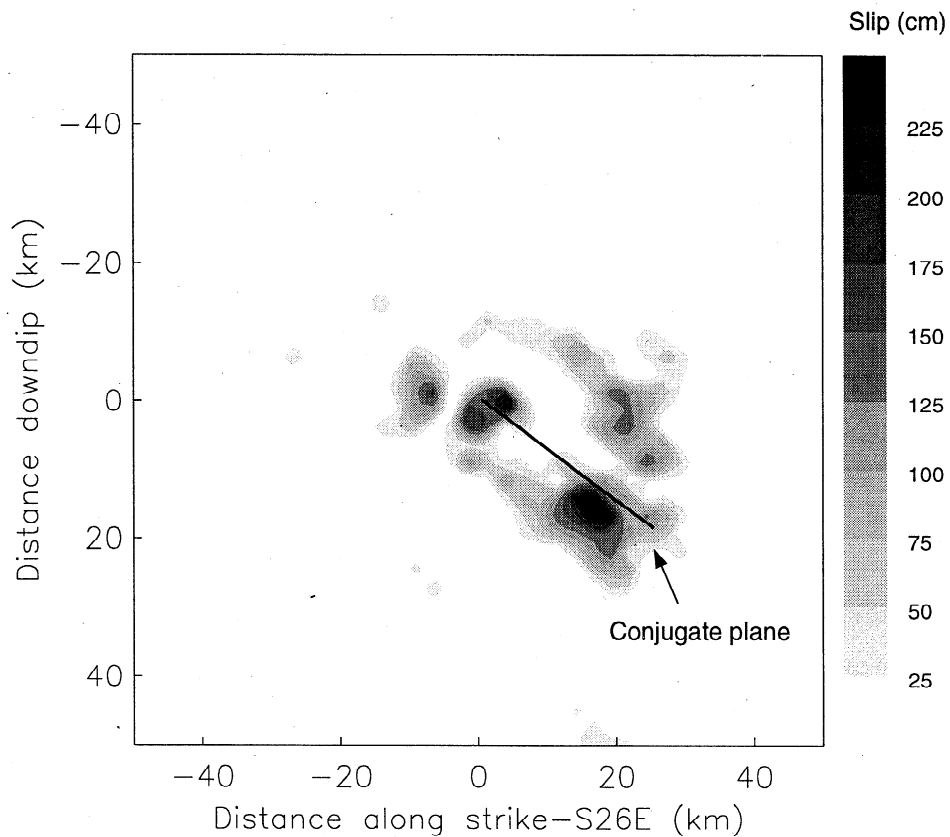
**Figure 16.** Slip model for the Japan Sea earthquake along the vertical fault plane. Slip concentrates near the intersection of the subhorizontal plane (solid line), which is an indication that rupture occurred on this plane.

of ~15%. Both the variance function and data misfit (norm of the residual vector) are plotted against the rupture velocity in Figure 24, and although the rupture velocity cannot be constrained on the basis of the variance, the misfit reaches its minimum value for high values of the rupture velocity close to the shear wave velocity. For the southward-dipping plane the data misfits appear to rule out values of the average rupture velocity much below 4.5 km s$^{-1}$. The synthetics in Figure 23 were computed from the solution for a rupture velocity of 5.1 km s$^{-1}$ and a rise time of 2 s. The better fit afforded by the southward-dipping plane is obvious for several of the time functions.
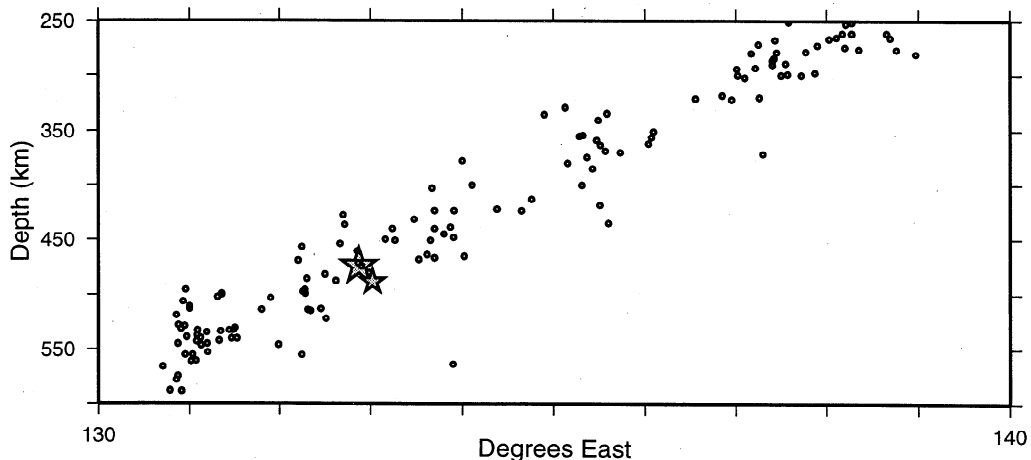
The preferred slip distribution is shown in Figure 25.



**Figure 17.** Cross section across the Japan slab at the latitude of the Japan Sea earthquake. Seismicity located within 5° of the cross section is shown. Large and small stars show location of the hypocenter and largest subevent of the Japan Sea earthquake, respectively.
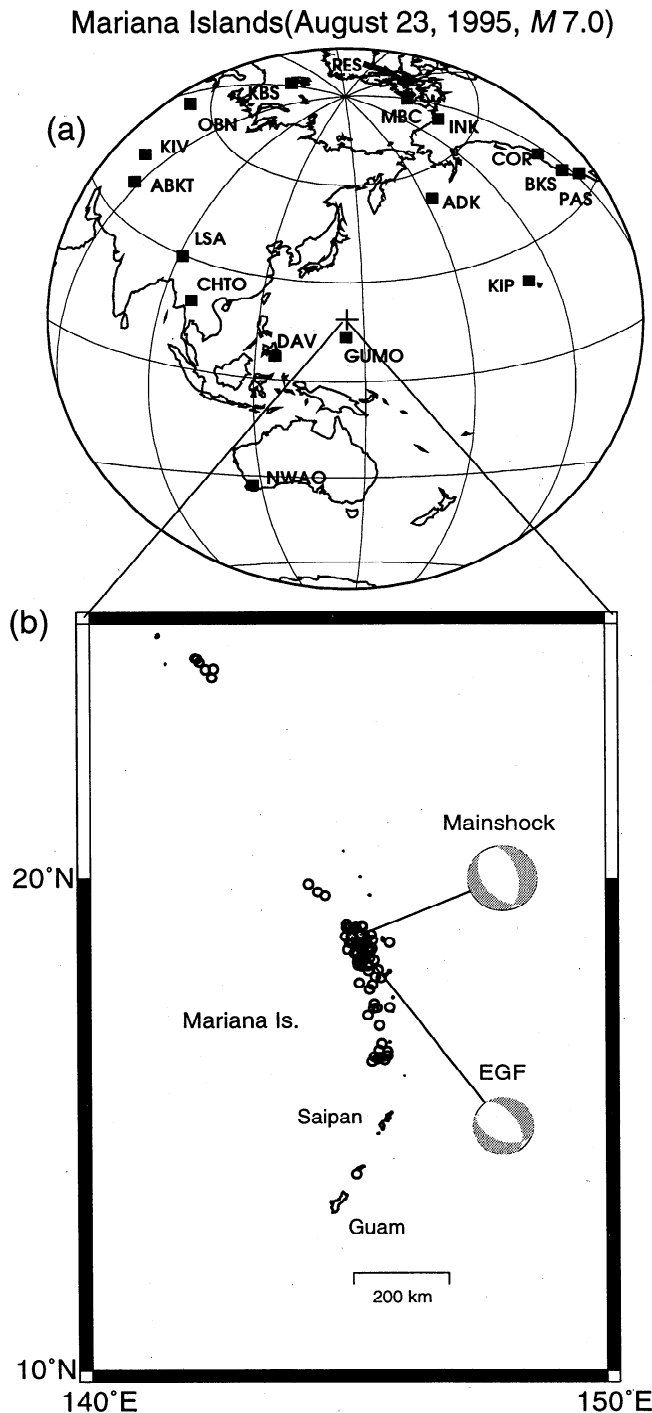
**Figure 18.** Map of region of the August 23, 1995, Mariana Islands deep earthquake showing background seismicity deeper than 450 km (circles) and focal mechanisms of the mainshock and aftershock used as an EGF. Note slight rotation in mechanism of the EGF relative to the mainshock. Figure 17a shows locations of stations used in the source inversion.

The total length of the rupture is about 120 km and extends laterally along strike to both the east and west. However, over two thirds of the moment was released to the west of the hypocenter. As indicated by the MRFs, the main moment release contained strong directivity

toward the northwest. It is also offset slightly to the south of the hypocenter. The total amounts of slip are low for such a small event, only slightly exceeding 1 m to the east of the hypocenter and reaching a maximum of only ~5 m. Thus the indicated stress drop is also not high, on the order of 10 MPa. Precise bounds on the stress drop cannot be obtained due to the inability of the inversion to place an upper bound on the rupture velocity. However, it is clear that this earthquake had a much different source process than the great Bolivian event, which occurred in a region of sparse background seismicity. On the basis of plate reconstructions, the age of the deep Nazca slab [*Engebretson and Kirby*, 1992] may be similar or slightly younger than that subducting beneath the Flores Sea.

Since the shape of the slip distribution for the Flores Sea earthquake strongly resembles the configuration of the trench immediately updip it is suggested that the moment release was contained within the slab core and possibly a wedge of metastable olivine. This could be the case if the deep slab is also buckled in a similar manner. Most of the moment release can be contained within a distance of 25 km along the slab dip. In addition, the larger afterhsocks of the event have been relocated by the joint hypocentral determination method [*Tinker et al.*, 1998] and are shown in Figure 25 projected onto the fault plane. The majority of the relocated afterhsocks occurred around the edges of the rupture, particularly the large area of moment release to the west of the hypocenter. The arc of slip on the southeast side of the rupture is likely an artifact of the solution, as we have seen in the above cases, and the lone event plotting in this region was probably not associated with rupture of the mainshock. The aftershock distribution therefore supports the interpretation that rupture was contained within the slab core. These results are consistent with those of *Goes et al.* [1997] who studied teleseismic *P* waves from the event. We also note that the northwestward directivity observed for the large area of slip to the west closely matches the initial strike obtained for the focal mechanism by *Tinker et al.* [1998] (130°), which therefore raises the possibility that faulting along a curved or along multiple fault planes caused the event. In this case we have the situation of a change in both the mechanism and the directivity along the fault plane; nevertheless, the facts mentioned above give us confidence in the results. The MRFs are surprisingly well fit considering these complications. The change in focal mechanism and directivity may contribute to the inability to place precise bounds on the rupture velocity.

### 5.5. August 5, 1996, Central Tonga earthquake

We next examined a large earthquake ($M_w$ 7.3) which occurred at a depth of 550 km within the central Tonga slab. The focal mechanism for this event (Figure 26) shows a combination of downdip compression with a significant component of shear deformation out of the
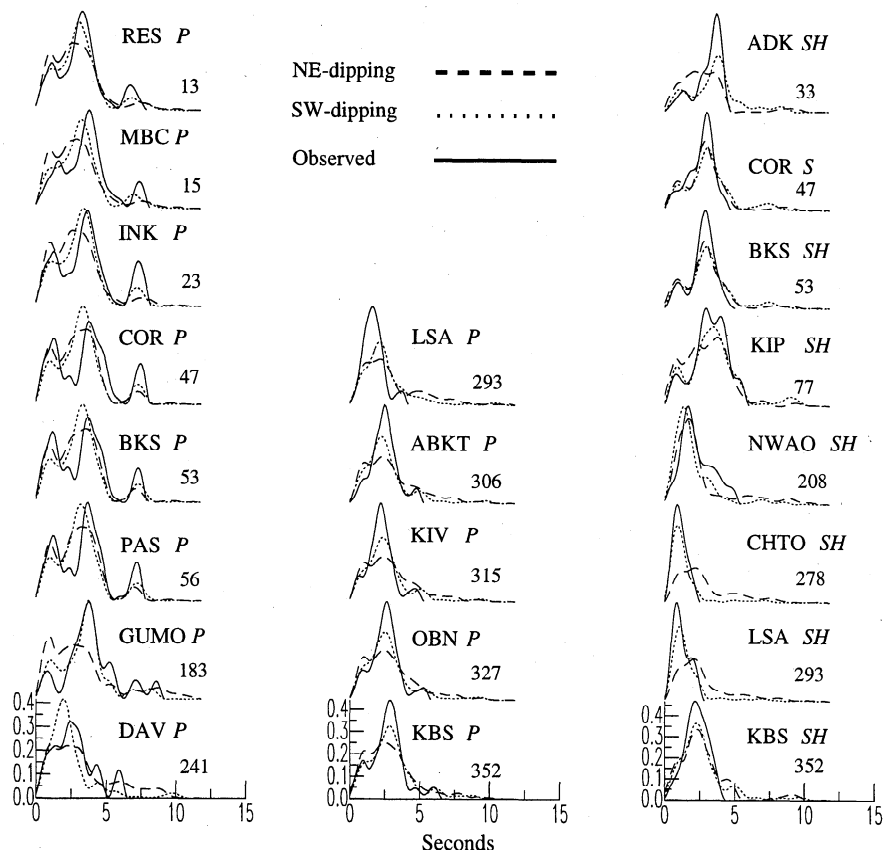
**Figure 19.** Data and synthetic MRFs for the Mariana Islands earthquake fault inversions. Azimuth and phase for each station are indicated. Solid traces are the observed MRFs, while dashed and dotted traces show synthetics for the NE- and SW-dipping planes, respectively. The SW-dipping fault plane is much more successful in predicting short durations at western azimuths, especially for the S waves.

plane of the Benioff zone. *Giardini and Woodhouse* [1986] have shown from the seismicity distribution that the Tonga slab is cut by a subhorizontal shear zone along which the deep portion (below 500-600 km depth) has been displaced some 500 km to the south during the last 9 Ma relative to the northern portion. This shear results from the combined northward movement of the Pacific and Australian plates relative to the lower mantle. They have found lineations of seismicity parallel to the shallow-dipping or subhorizontal nodal plane for this type of mechanism in the region. The CMT solution indicates a strike of 217° and a dip of 20° for this plane. Although a number of events with a similar focal mechanism have occurred in the area within the last 5-10 years, none were large enough to be well recorded teleseismically and thus we have estimated the MRFs for this earthquake using theoretical Green's functions. Very few large aftershocks were produced by the event.

A data set consisting of 30 P and S wave MRFs was inverted for this earthquake, shown in Figure 27. The fault grid for the inversion consisted of 50 cells in each dimension for a total length of 150 km. Most of the MRFs resemble simple triangles in shape, with an av-

erage duration of ~9 s. No azimuth shows a consistent short duration, although the early, sharp peak observed in the MRFs for stations to the north and northeast suggests a component of rupture directivity in that direction. The best solutions for both fault planes (Figure 28) show this feature. For the subhorizontal fault plane the main moment release consists of three separate subevents containing very large slip amounts separated from each other by 5-10 km. The largest subevent lies to the north for which a peak slip of over 15 m is obtained. Again, there are arcuate outlying regions of low-level slip which are likely artifacts. The vertical nodal plane concentrates most of the slip in a thin, narrow band with a shallow dip and having a maximum slip amplitude of 18 m. This favors the subhorizontal plane as the true rupture plane, although this band of slip is offset slightly above the hypocenter location. A smaller subevent occurs downdip as well as a diffuse area of slip at shallower depths and extending 15 km along strike to the southwest. If we ignore the outlying slip artifacts, the rupture area is clearly extremely compact, especially for the subhorizontal plane.
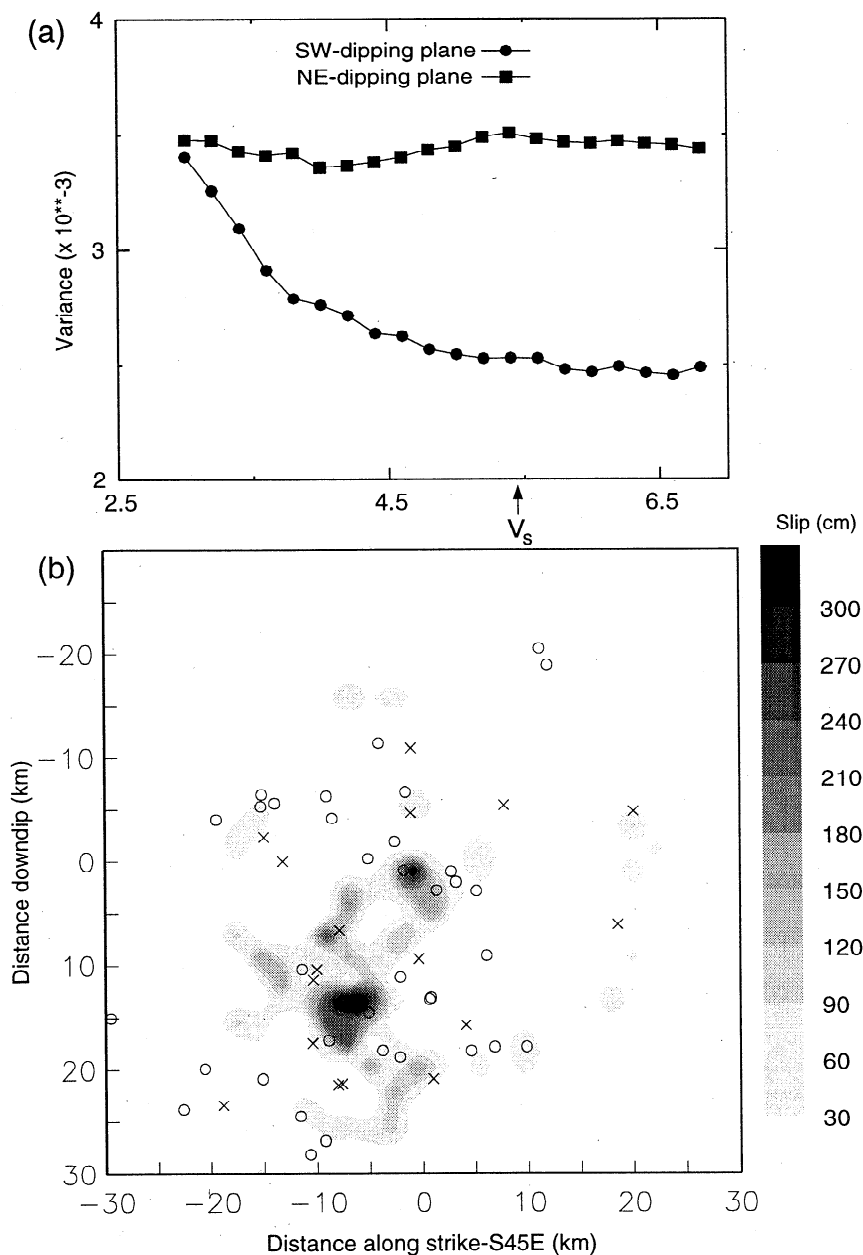
As Figure 29 shows, the subhorizontal plane gives a

**Figure 20.** (a) Variance curves for inversion along both nodal planes for the Mariana Islands earthquake. The difference between the planes is quite significant and is evident in the data fits. Rupture velocity is not well constrained as values higher than about 4.5 km s$^{-1}$ result in equal or lower variance. The shear velocity ($v_s$) at this depth is about 5.4 km s$^{-1}$. (b) Output slip solution along the SW-dipping plane for the Mariana Islands earthquake (rupture velocity 5.0 km s$^{-1}$). Westward rupture directivity is evident. Background seismicity deeper than 500 km projected onto the fault plane is shown as the circles and aftershock locations are shown as crosses.

solution having a consistently lower variance. This difference is not great (75% confidence level), although we believe that the other factors discussed above and below indicate that rupture probably occurred on the subhorizontal plane. The better fit to the data afforded by this plane is evident at only a few of the stations as the synthetic MRFs are very similar for either model. The most significant differences are for the $S$ waves at stations to the north and west. Neither model fits the shorter duration observed for Palmer Station, Antarctica (PMSA). The average rupture velocity appears to be in the range 3.2-4.5 km s$^{-1}$ with much lower values than this resulting in significant degradation to the data fits. With these values we estimate the static stress drop to lie in the range 10-24 MPa. However, if the moment release was confined only to the area of the three large
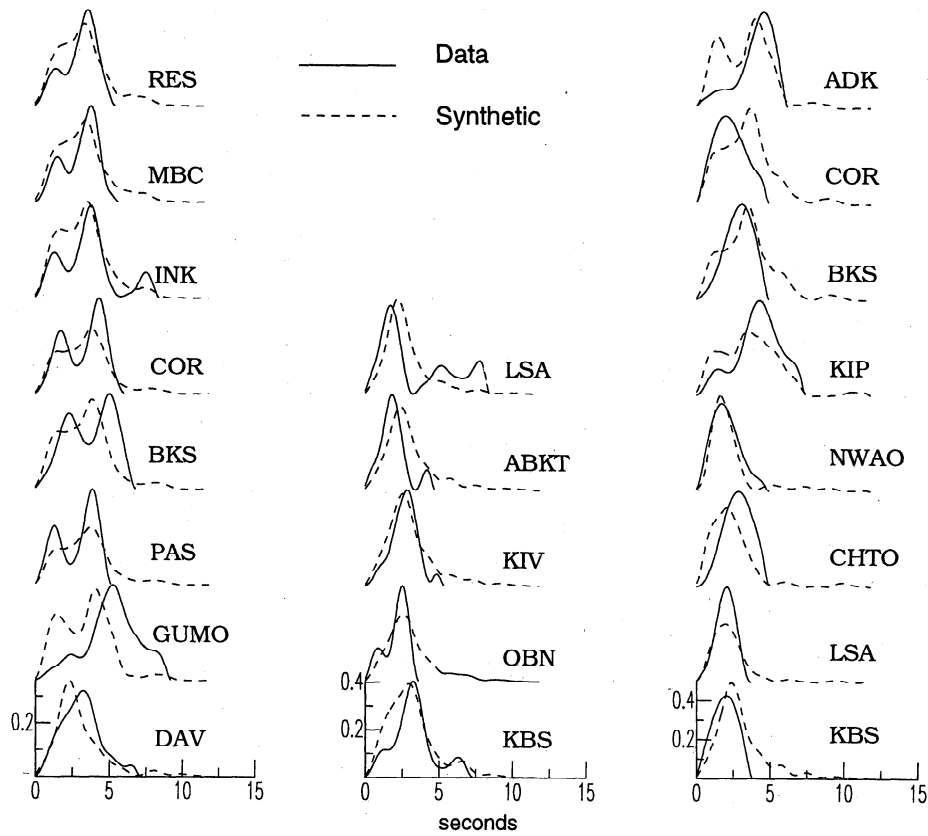
**Figure 21.** Comparison between MRFs calculated from deconvolution using theoretical Green's functions (solid) and predicted MRFs from fault inversion (dashed) of these data. Phases are the same as in Figure 19. Traces were low-pass filtered at 0.5 Hz. The shape of several MRFs is changed, especially at station GUMO
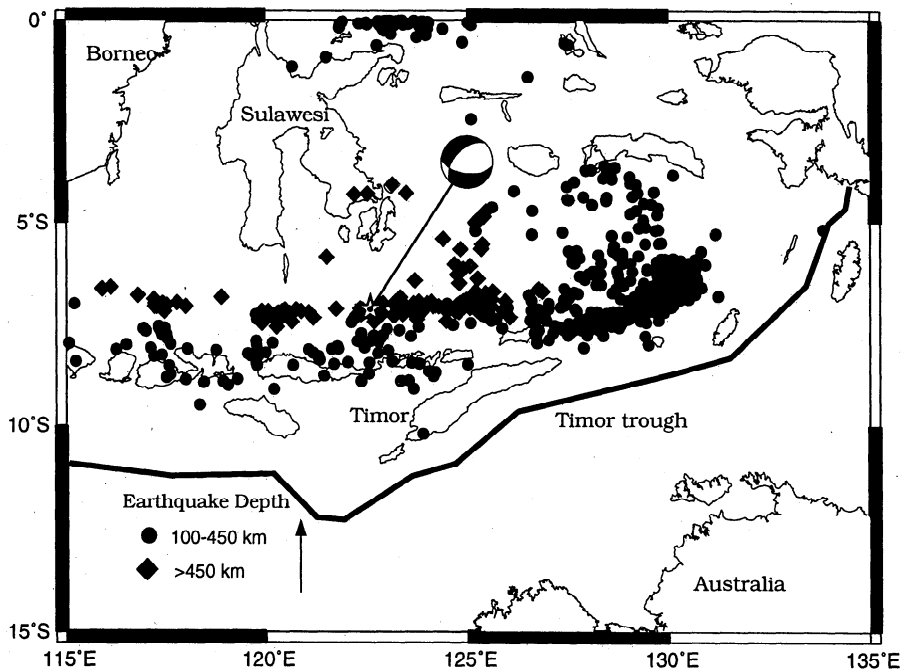


**Figure 22.** Map showing location of the June 17, 1996, Flores Sea deep earthquake and background seismicity. The location of the Java trench-Timor trough is indicated by the thick line. The Flores Sea event is located immediately downdip of an arcward concave kink in the strike of the Java trench (indicated by the arrow). Different symbols indicate different depth ranges for the seismicity.
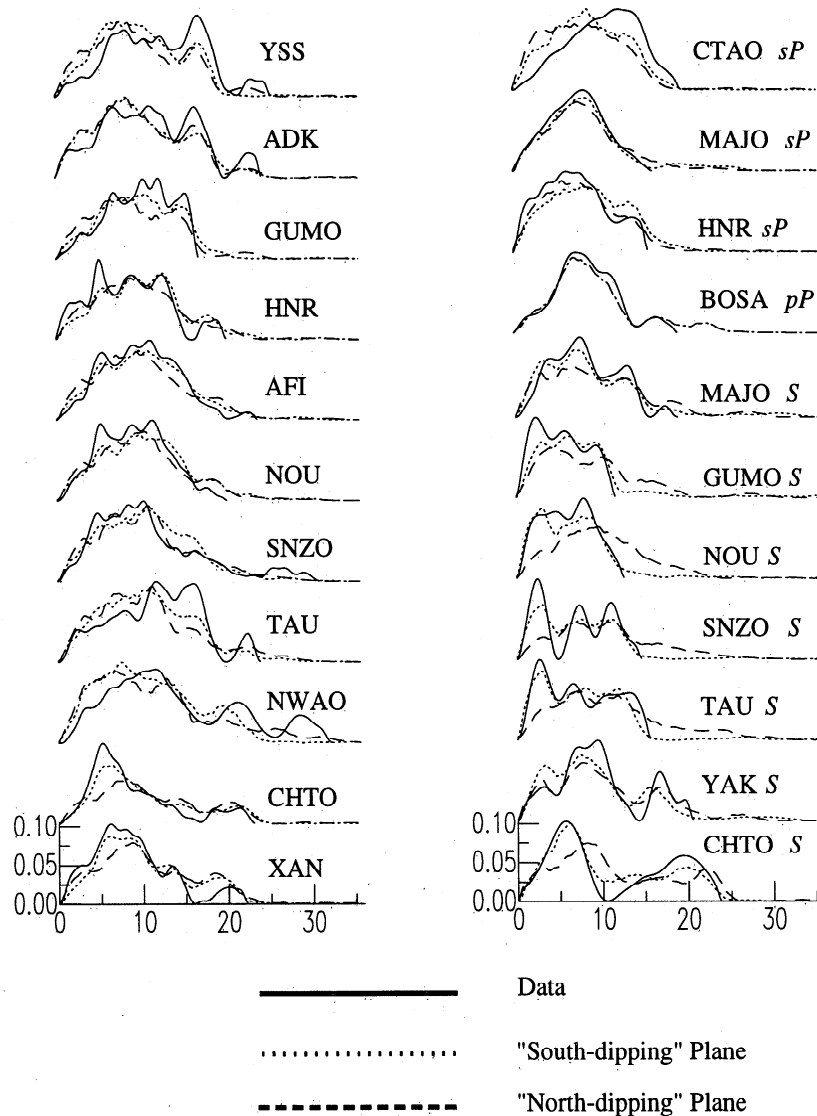
Data

................. "South-dipping" Plane

------------ "North-dipping" Plane

**Figure 23.** Comparison of observed (solid traces) with synthetic MRFs for source inversion of the Flores Sea earthquake. Improvement in fit for the south-dipping fault plane is evident in several of the phases. All traces were low-pass filtered with a corner at 0.2 Hz.

subevents, the average stress drop could have been as high as 60 MPa.

One other observation which points toward the subhorizontal slip model as representing the true slip model is the background seismicity distribution. Projected onto both slip distributions in Figure 28 are the locations of events with $m_b > 5.0$ occurring deeper than 500 km. The three subevents evident in Figure 28a are aligned almost exactly with the seismicity, and the moment release, especially that of the larger northern subevent, appears to be nearly surrounded by events. Thus we infer that moment release was completely contained within the slab core. The seismicity becomes more diffuse toward the north. This is consistent with the larger size of the northern subevent and suggesting that the slab broadens in this direction. Total thickness of the seismogenic zone appears to be about 20 km. As

the vertical plane lies at an angle to the strike of the Benioff zone, the moment release for this solution would extend outside of the active seismic zone if the diffuse area of slip above the hypocenter is assumed to be real.

## 6. Discussion

### 6.1. Rupture Velocity and Stress Drop

A summary of the source parameters for the events studied in this paper is presented in Table 3. Accumulated evidence from a number of studies indicates that deep earthquakes are characterized by a wide variability of the source parameters, even for events occurring within the same subduction zone. For example the rupture velocity of the Bolivia mainshock was only about half that of the January 10, 1994, foreshock. Most of
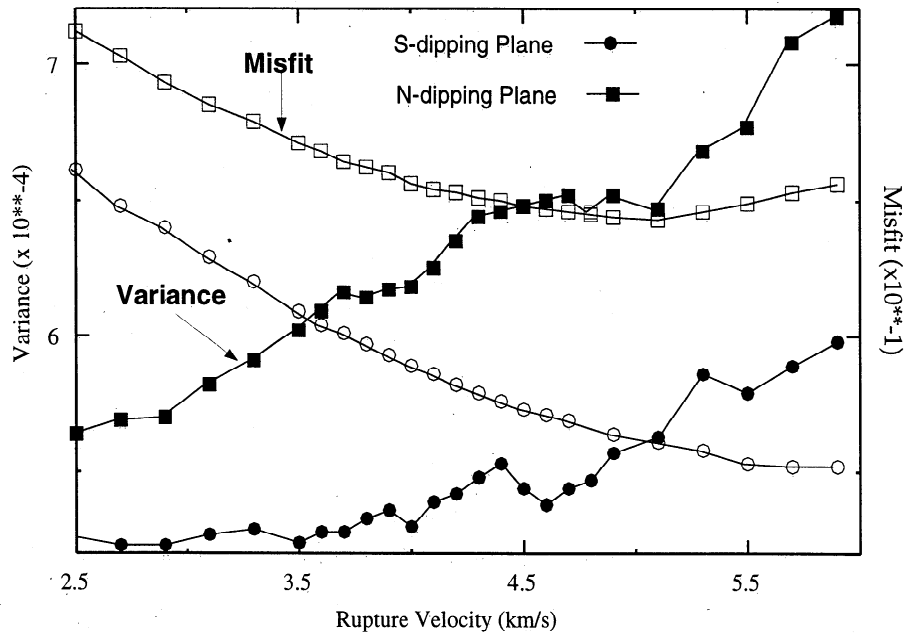
**Figure 24.** Data misfit (open symbols) and variance (solid symbols) for inversions of the Flores Sea earthquake. Although the data misfit continually decreases with increasing rupture velocity, the variance (calculated from (5)) increases because of the normalization by the number of free parameters.
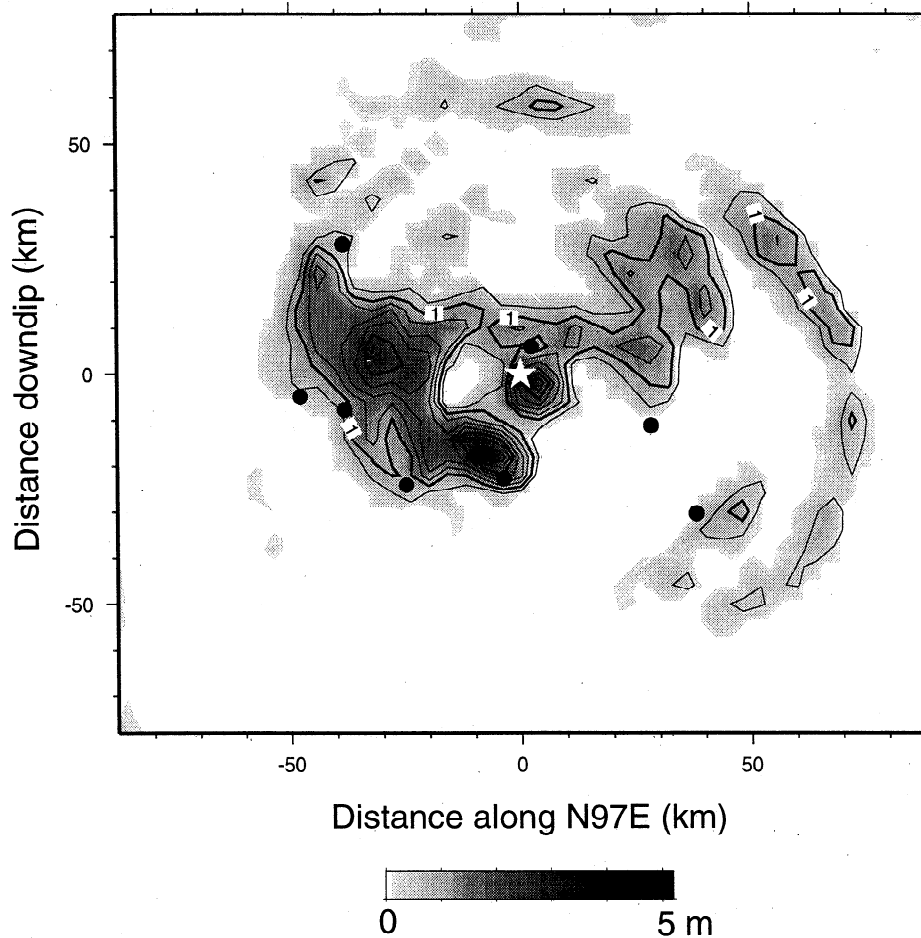


**Figure 25.** Slip model for the Flores Sea earthquake along the south-dipping plane with a rupture velocity of 5.1 km s$^{-1}$. The contour interval is 0.5 m. The hypocenter is shown as the star and aftershock locations [from *Tinker et al.*, 1998] are projected onto the fault plane as the black filled circles.
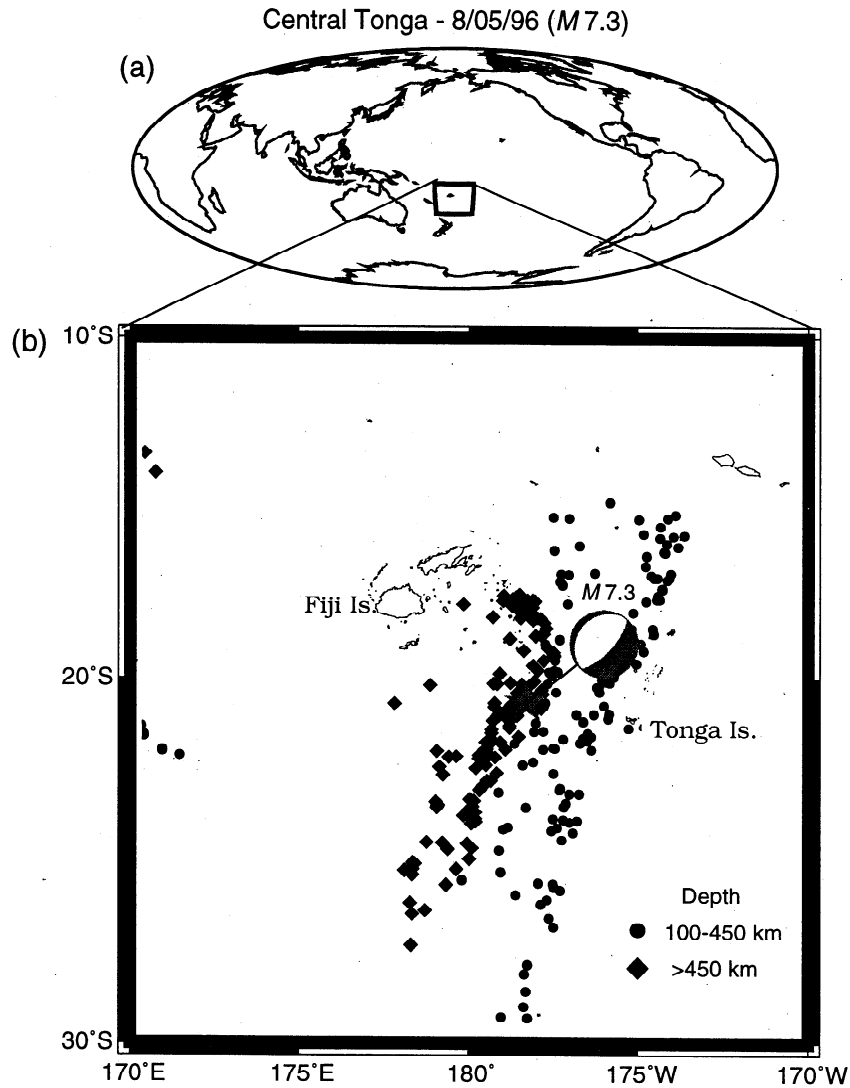
**Figure 26.** Map of the source region of the August 5, 1996, Tonga deep earthquake along with intermediate depth and deep background seismicity.

these events exhibit average rupture velocities substantially less than the shear wave velocity but varying over a wide range. There is no clear indication as to the preferred propagation velocity for a transformational fault or for any of the other faulting mechanisms proposed to account for deep-focus earthquakes, except that it should be less than the shear wave velocity. Any viable rupture mechanism must be able to explain the extremely low rupture velocity of the Bolivia mainshock as well as values close to the shear wave velocity.

The complex nature of deep-focus earthquakes is clearly evident in these results. The slip distributions for these events show very concentrated areas of moment release separated by regions of little or no slip. In this regard the ruptures of deep-focus earthquakes resemble those of shallow earthquakes. As a result, the stress drop estimates are even larger than would have been expected from the overall small source dimensions for these events. Particularly it is suggested that stress

drop estimates from aftershock distributions are likely to be substantially too low. Stress drops for some deep earthquakes (e.g., Flores Sea, 1994 Fiji Islands) are similar to those normally observed for shallow events (1-10 MPa). However, values for the other events in this study are generally much higher. Thus a tendency for deep-focus earthquakes to exhibit higher static stress drops than shallow events is supported by these data.

### 6.2. Slip Patterns and Rupture Mechanisms

Background seismicity and aftershock distributions, as well as other considerations, suggest that most or all of the moment release for these events occurred within the active seismic slab. In fact, only for two earthquakes, the 1994 Fiji Islands and Bolivia events, has convincing evidence to the contrary been presented, and even these events show substantial decrease in slip in areas outside of the slab core. Thus the locations of slabs in areas where background seismicity is sparse
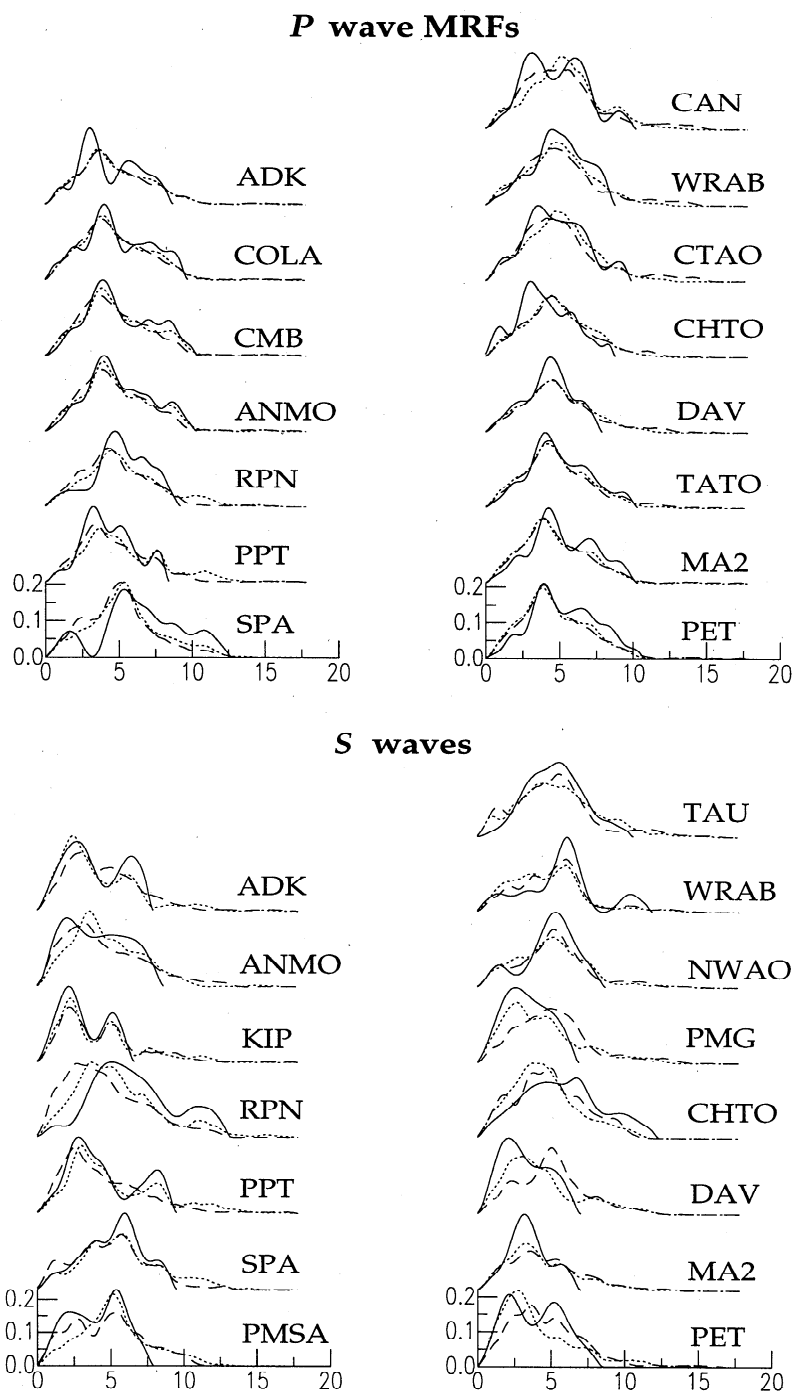
## P wave MRFs

## S waves

**Figure 27.** Comparison of observed MRFs (solid) with synthetics for inversions of the central Tonga earthquake. Dashed curves are for the best near-vertical plane solution and dotted curves are for the best horizontal plane solution. All traces were low-pass filtered at 1 Hz.

may potentially be determined by mapping the moment release in large events. This further supports the transformational faulting mechanism or other temperature-controlled processes such as instabilities associated with plastic deformation [*Hobbs and Ord*, 1988] as the cause of most deep-focus earthquakes. The preferential occurrence of aftershocks within the slab core [*Wiens et al.*, 1994] or the existence of double seismic zones [*Iidaka and Furukawa*, 1994; *Wiens et al.*, 1993] are also diffi-

cult to explain without invoking some mechanism controlled by a critical temperature.

On the other hand, it is likely that mechanisms other than transformational faulting are necessary to explain rupture of the Fiji and Bolivia events through the slab core. Although some have argued that the metastable olivine wedge may become thickened through slab parallel compressive stress in regions where a kink exists [e.g., *Kirby et al.*, 1995a], it is not totally clear how
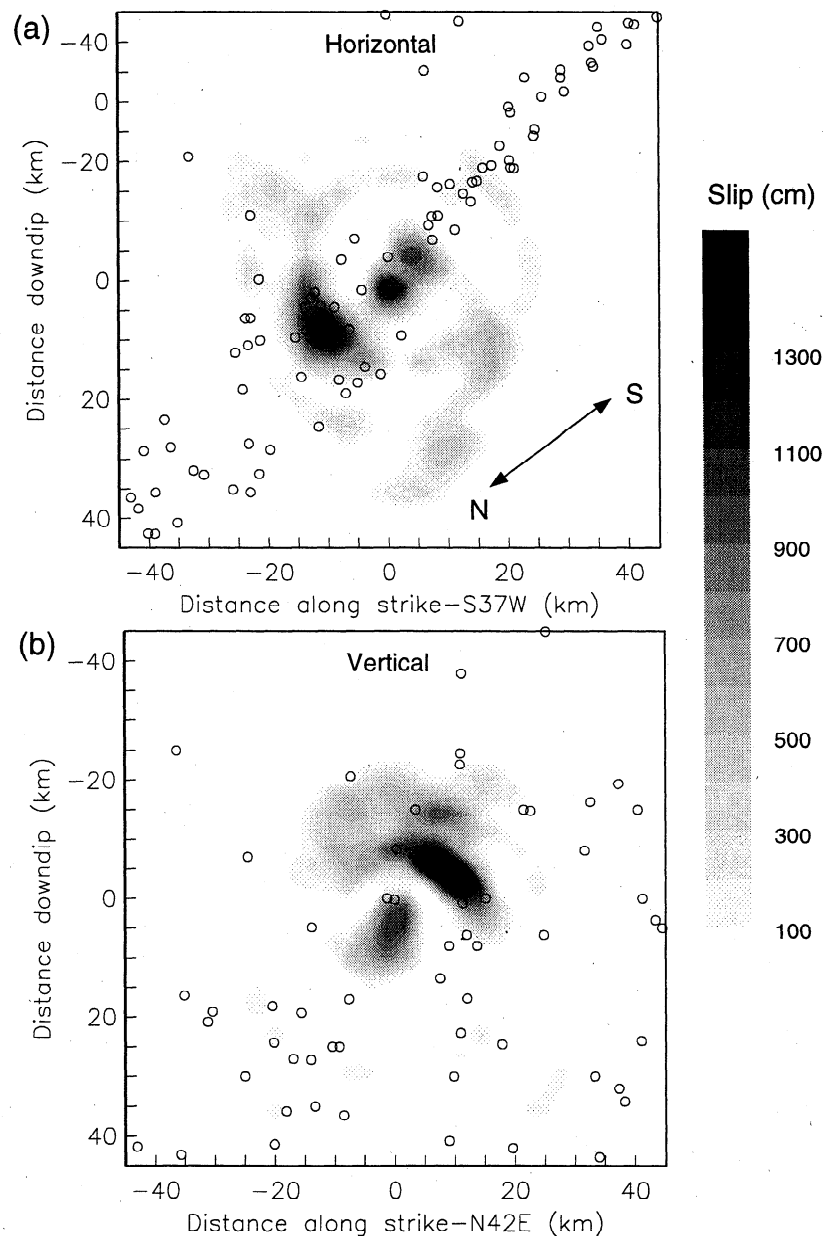
**Figure 28.** Best fitting slip distributions for the Tonga earthquake along (a) the horizontal plane and (b) the near-vertical plane. Background seismicity is shown projected onto the fault plane. For Figure 28a only events between 500 and 650 km depth are shown.

such a process might take place or why a thickened slab core is not observed in the aftershock distribution [*Myers et al.*, 1995]. Nevertheless, the occurrence of three of the largest historical deep events in regions of slab kinks (this is also true for the 1970 Colombian event) provides support for this hypothesis.

One other possible mechanism for extending rupture into the aseismic mantle surrounding the slab is shear induced melting. This possibility has been advanced by *Ogawa* [1987] and recently revived by *Kikuchi and Kanamori* [1994] with regard to the great Bolivian earthquake. *Ogawa* [1987] has even suggested that shear-induced melting may occur within a slab at real-

istic strain rates without the occurrence of phase transitions. In his model, instability is enhanced by the presence of localized shear zones. This may suggest a role for preexisting failure planes in generating deep earthquakes, such as is suggested by *Silver et al.* [1995] for the Bolivian event. They propose dehydration of hydrous minerals within these shear planes as the cause. However, simple brittle rupture on a weakened shear plane does not seem as capable of explaining the wide range of observed rupture velocities as a rupture controlled by transient thermal processes. It is interesting that the two largest recent deep events, Bolivia and Flores Sea, appear somewhat different than the smaller
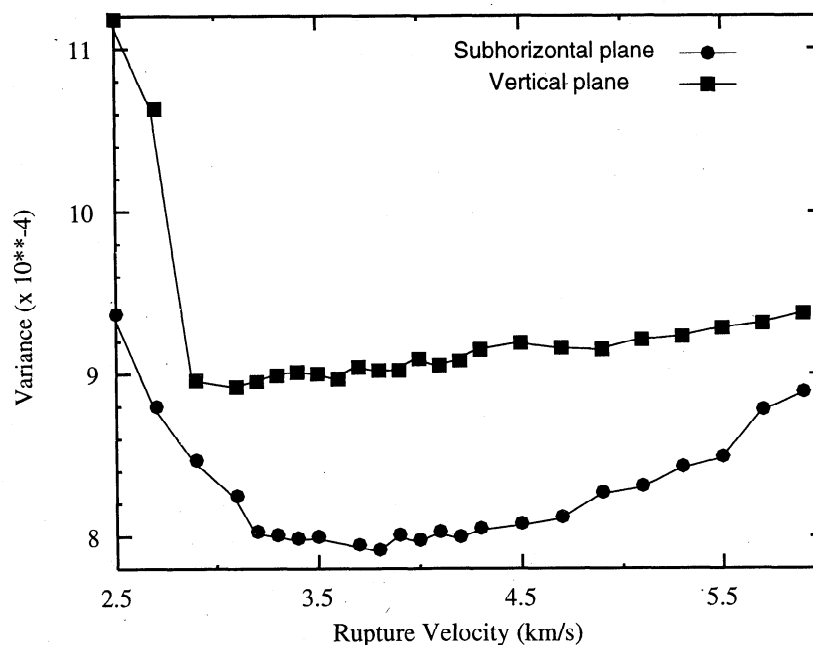
**Figure 29.** Variance curves for the inversion of the Tonga earthquake.

events in this study in that the principal portion of the moment release appears to consist of a continuous patch rather than isolated subevents separated by regions of little or no slip. This would suggest that shear heating instabilites may be more likely associated with the rupture process of Bolivia and Flores Sea than the other events, as it would not be likely that such instabilites could reinitiate so quickly over length scales of tens of kilometers. Thus it would seem that the shear heating mechanism is a better candidate to sustain rupture rather than initiate it.

In summary, it would appear that the available data favor a complex process involving two or more mechanisms, occurring either together or perhaps varying between subduction zones according to thermal state. This is further supported by variations in $b$ value and aftershock populations between subduction zones with different thermal parameters [*Wiens and McGuire*, 1995]. It may be that small to moderate sized events are the result of phase transitions and that the rare, large event

occurs as the result of one of the other processes described above. The stress redistribution from the latter mechanism must then be capable of triggering phase transitions within the slab to explain the distribution of aftershocks. The combination of more than one mechanism may help explain why deep earthquakes tend to have fewer aftershocks [*Frohlich*, 1987], why aftershocks do not preferentially cluster along the mainshock fault plane [*Willemann and Frohlich*, 1987], and why the observed source parameters are so variable.

We have observed a tendency for horizontal rupture propagation during these events. With the exception of the Mariana Islands earthquake all of these events rupture either along a sub-horizontal fault plane or largely horizontally along a more steeply dipping fault plane. This results in a much greater source dimension in the horizontal direction than the vertical direction. Studies of the rupture history of the great 1970 Colombian earthquake [e.g., *Furumoto*, 1977; *Estabrook*, 1997] suggest a similar pattern, and *Glennon and Chen* [1993]

**Table 3.** Estimated Source Parameters

| Event | Depth | $M_w$ | $V_r$ | $\Delta\sigma$ | $A_r$ | $u_{max}$ | $\bar{u}$ |
|-------|-------|-------|-------|----------------|-------|-----------|-----------|
| 1 | 596 | 7.0 | 2.5-4.8 | 5-15 | 3-5 | 1.0-2.0 | 0.25-1.0 |
| 2 | 471 | 7.3 | 4.0-5.0 | 12-30 | 4-7 | 1.5-3.0 | 0.5-1.0 |
| 3 | 595 | 7.0 | >3.5 | 20-48 | 1.7-3.0 | ~3.5 | ~1.5 |
| 4 | 587 | 7.9 | >4.5 | ~10 | >20 | 4-6 | ~1.5 |
| 5 | 550 | 7.3 | 3.2-4.5 | 10-24 | 6-10 | 12-18 | 4-8 |

$V_r$ is rupture velocity (km s$^{-1}$), $A_r$ is the rupture area ($10^2$ km$^2$), $\Delta\sigma$ is the stress drop (MPa), and $u_{max}$ and $\bar{u}$ (m) are the peak and average slip, respectively. Rupture area was calculated by including portions of the rupture with > 5% peak slip. Events are the same as those listed in Table 1.

have observed subhorizontal ruptures for other deep earthquakes in the northwest Pacific. This may be indicative of an isobaric process constraining the vertical propagation of the rupture. It is unclear why transformational faulting would favor such a rupture geometry. A large component of differential horizontal flow at the base of the upper mantle, perhaps because of layered convection, might explain a preference for rupture on subhorizontal surfaces. Although contortions in the configuration of slabs as they approach the 660 km discontinuity, particularly in the Tonga and Indonesian slabs, have been interpreted as evidence of resistance to lower mantle penetration [*Lundgren and Giardini*, 1994], there is also much evidence that slabs penetrate into the lower mantle [e.g., *van der Hilst et al.*, 1991; *Grand et al.*, 1997]. Large pulses of horizontal flow might therefore be episodic, perhaps even causing periods of accelerated global moment release in deep-focus earthquakes similar to that which began in 1994.

Finally, the question remains as to the method of stress transfer across areas of the rupture where little or no slip is observed. Resolution of the inversion method does not make it possible to say with certainty that no slip exists in these regions. However, it is rather more likely that the inversion will place slip in areas where none exists than the reverse, as is shown in the synthetic tests. If indeed there is an absence of slip in these areas, then this raises the possibility that these events are occurring on multiple fault planes. Such an interpretation has been made by *Kuge and Kawakatsu* [1990] for a "non-double couple" deep earthquake. Stress may be transferred through aseismic slip or dynamically by the passage of seismic waves through the region. The aseismic creep hypothesis might potentially explain the low propagation speed observed for the 1994 great Bolivian earthquake; however, for speeds close to the shear wave velocity this is unlikely. Rather, the dynamic triggering of multiple events is more likely, probably during passage of the $S$ wave from the initial rupture. Under the transformational faulting hypothesis, large jumps in the rupture may be explained by prior transformation of olivine within the low-slip areas. Disjointed or isolated regions of metastable olivine would be particularly prone to dynamical triggering [*Kirby et al.*, 1995b].

## 7.  Summary

Rupture histories of five recent large, deep-focus earthquakes have been determined by a method which inverts for fault slip using moment rate functions determined from teleseismic body wave phases. Use of different phase types is important for resolving the causative fault plane and other rupture parameters. Either theoretical or empirical Green's functions can be used for the deconvolutions, although there is a tradeoff between adequate knowledge of near-source structure and possible problems resulting from source finiteness of the Green's function event. Tests carried out using synthetic data

indicate that details of the slip process may be recovered under a variety of conditions. These tests indicate the manner in which certain complicating factors limit the usefulness of the method, and the results from applications to real data have been interpreted on the basis of information gleaned from the synthetic tests.

Source parameters for the events studied exhibit wide variability. This evidence, as well as a growing body of evidence from other studies, suggests that multiple mechanisms may be responsible for deep-focus earthquakes. Static stress drops are in general larger than those estimated for shallow earthquakes and may be significantly underestimated if the source area is determined from the spatial distribution of discrete subevents [see also *Ihmlé*, 1998] or from aftershock locations.

Moment release for large, deep-focus earthquakes appears to be largely confined to the slab core, with few exceptions. This strongly suggests that a process controlled by a critical temperature plays a large part in the rupture propagation of even the largest deep events. As yet unexplained is a tendency for horizontal rupture propagation observed for these events.

## References

Antolik, M., New results from studies of three outstanding problems in local, regional, and global seismology, *Ph.D. thesis*, 311 pp., Univ. of Calif., Berkeley, 1996.

Antolik, M., D. Dreger, and B. Romanowicz, Finite fault source study of the great 1994 deep Bolivia earthquake, *Geophys. Res. Lett., 23*, 1589-1592, 1996.

Ben-Menahem, A., and S.J. Singh, *Seismic Waves and Sources*, Springer-Verlag, New York, 1981.

Cardwell, R.K., and B.L. Isacks, Geometry of the subducted lithosphere beneath the Banda Sea in eastern Indonesia from seismicity and fault plane solutions, *J. Geophys. Res., 83*, 2825-2838, 1978.

Chen, W.-P., L.-R. Wu, and M.A. Glennon, Characteristics of multiple ruptures during large deep-focus earthquakes, in *Subduction: Top to Bottom*, Geophys. Monogr., vol. 96, edited by G. Bebout et al., pp. 357-368, AGU, Washington, D.C., 1996.

Chung, W.-Y., and H. Kanamori, Variation of seismic source parameters and stress drops within a descending slab and its implications in plate mechanics, *Phys. Earth Planet. Inter., 23*, 134-159, 1980.

Clayton, R.W., and R.A. Wiggins, Source shape estimation and deconvolution of teleseismic body waves, *Geophys. J. R. Astron. Soc., 47*, 151-177, 1976.

Das, S., and P. Suhadolc, On the inverse problem for earthquake rupture: The Haskell-type source model, *J. Geophys. Res., 101*, 5725-5738, 1996.

DeMets, C., R.G. Gordon, D.F. Argus, and S. Stein, Current plate motions, *Geophys. J., 101*, 425-478, 1990.

Dreger, D.S., Empirical Green's function study of the Jan-

uary 17, 1994 Northridge, California, earthquake, *Geophys. Res. Lett., 21,* 2633-2636, 1994.

Durek, J.J., and G. Ekström, A radial model of anelasticity consistent with long-period surface wave attenuation, *Bull. Seismol. Soc. Am., 86,* 144-158, 1996.

Engebretson, D.C., and S.H. Kirby, Deep Nazca slab seismicity: Why is it so anomalous?, *Eos Trans. AGU, 73*(43), Fall Meet. Suppl., 379, 1992.

Estabrook, C.H., Another look at great South American deep earthquakes: results from body wave inversion, *Eos Trans. AGU, 78*(46), Fall Meet. Suppl., F450, 1997.

Estabrook, C.H., and G. Bock, Rupture history of the great Bolivian earthquake: Slab interaction with the 660-km discontinuity?, *Geophys. Res. Lett., 22,* 2277-2280, 1995.

Frohlich, C., Aftershocks and temporal clustering of deep earthquakes, *J. Geophys. Res., 92,* 13,944-13,957, 1987.

Frohlich, C., The nature of deep earthquakes, *Annu. Rev. Earth Planet. Sci., 17,* 227-254, 1989.

Fukao, Y., and M. Kikuchi, Source retrieval for mantle earthquakes by iterative deconvolution of long-period P waves, *Tectonophysics, 144,* 249-269, 1987.

Furumoto, M., Spatio-temporal history of the deep Colombia earthquake of 1970, *Phys. Earth Planet. Inter., 15,* 1-12, 1977.

Giardini, D., and J.H. Woodhouse, Horizontal shear flow in the mantle beneath the Tonga arc, *Nature, 319,* 551-555, 1986.

Glennon, M.A., and W.-P. Chen, Systematics of deep-focus earthquakes along the Kuril-Kamchatka arc and their implications on mantle dynamics, *J. Geophys. Res., 98,* 735-769, 1993.

Glennon, M.A., and W.-P. Chen, Ruptures of deep-focus earthquakes in the northwestern Pacific and their implications on seismogenesis, *Geophys. J. Int., 120,* 706-720, 1995.

Goes, S., and J. Ritsema, Broadband P wave analysis of the large deep Fiji Island and Bolivia earthquakes of 1994, *Geophys. Res. Lett., 22,* 2249-2252, 1995.

Goes, S., L. Ruff, and N. Winslow, The complex rupture process of the 1996 deep Flores, Indonesia, earthquake ($M_w = 7.9$) from teleseismic P waves, *Geophys. Res. Lett., 24,* 1295-1298, 1997.

Grand, S.P., R. van der Hilst, and S. Widiyantoro, Global seismic tomography: Snapshot of convection in the Earth, *GSA Today, 7*(4), 1-7, 1997.

Hartog, R., and S. Schwartz, Directivity analysis of the December 28, 1994 Sanriku-Oki earthquake ($M_w$ 7.7), *Geophys. Res. Lett., 23,* 2037-2040, 1996.

Hartzell, S., G.S. Stewart, and C. Mendoza, Comparison of $L_1$ and $L_2$ norms in a teleseismic waveform inversion for the slip history of the Loma Prieta, California, earthquake, *Bull. Seismol. Soc. Am., 81,* 1518-1539, 1991.

Hobbs, B.E., and A. Ord, Plastic instabilities: Implications for the origin of intermediate and deep-focus earthquakes, *J. Geophys. Res., 93,* 10,521-10,540, 1988.

Houston, H., Deep earthquakes shake up debate, *Nature, 372,* 724-725, 1994.

Ihmlé, P.F., On the interpretation of subevents in teleseismic waveforms: The 1994 Bolivia deep earthquake revisited, *J. Geophys. Res., 103,* 17,919-17,932, 1998.

Iidaka, T., and Y. Furukawa, Double seismic zone for deep earthquakes in the Izu-Bonin subduction zone, *Science, 263,* 1116-1118, 1994.

Kennett, B.L.N., and E.R. Engdahl, Traveltimes for global earthquake location and phase identification, *Geophys. J. Int., 105,* 429-465, 1991.

Kikuchi, M., and M. Ishida, Source retrieval for deep local earthquakes with broadband records, *Bull. Seismol. Soc. Am., 83,* 1855-1870, 1993.

Kikuchi, M., and H. Kanamori, The mechanism of the deep Bolivia earthquake of June 9, 1994, *Geophys. Res. Lett., 21,* 2341-2344, 1994.

Kirby, S.H., W.B. Durham, and L.A. Stern, Mantle phase changes and deep earthquake faulting in subducting lithosphere, *Science, 252,* 216-225, 1991.

Kirby, S.H., E.A. Okal, and E.R. Engdahl, The 9 June 94 Bolivian deep earthquake: An exceptional event in an extraordinary subduction zone, *Geophys. Res. Lett., 22,* 2233-2236, 1995a.

Kirby, S.H., E.A. Okal, and E.R. Engdahl, Ultra-large, very deep earthquakes: Dynamical triggering of transformational faults in isolated regions of grossly metastable peridotite?, *Eos Trans. AGU, 76,* 606-607, 1995b.

Kuge, K., and H. Kawakatsu, Analysis of a deep "non-double couple" earthquake using very broadband data, *Geophys. Res. Lett., 17,* 227-230, 1990.

Lundgren, P., and D. Giardini, Lateral structure of the subducting Pacific plate beneath the Hokkaido corner from intermediate and deep earthquakes, *Pure Appl. Geophys., 134,* 386-404, 1990.

Lundgren, P., and D. Giardini, Seismicity, shear failure, and modes of deformation in deep subduction zones, *Phys. Earth Planet. Inter., 74,* 63-74, 1992.

Lundgren, P., and D. Giardini, Isolated deep earthquakes and the fate of subduction in the deep mantle, *J. Geophys. Res., 99,* 15,833-15,842, 1994.

McGuire, J.J., D. Wiens, P. Shore, and M. Bevis, The March 9, 1994 ($M_w$ 7.6) deep Tonga earthquake: Rupture outside the seismically active slab, *J. Geophys. Res., 102,* 15,163-15,182, 1997.

Mori, J., and S. Hartzell, Source inversion of the 1988 Upland earthquake: Determination of a fault plane for a small event, *Bull. Seismol. Soc. Am., 80,* 507-518, 1990.

Myers, S.C., T. Wallace, S. Beck, P. Silver, G. Zandt, J. Vandecar, and E. Minaya, Implications of spatial and temporal development of the aftershock sequence for the $M_w$ 8.3 June 9, 1994, deep Bolivian earthquake, *Geophys. Res. Lett., 22,* 2269-2272, 1995.

Ogawa, M., Shear instability in a viscoelastic material as the cause of deep-focus earthquakes, *J. Geophys. Res., 92,* 13,801-13,810, 1987.

Ruff, L.J., Tomographic imaging of the earthquake rupture process, *Geophys. Res. Lett., 11,* 629-632, 1984.

Saraó, A., S. Das, and P. Suhadolc, Effect of non-uniform station coverage on the inversion for earthquake rupture history for a Haskell-type source model, *J. Seismol.,* in press, 1998.

Silver, P.G., S. Beck, T. Wallace, and C. Meade, Rupture characteristics of the deep Bolivian earthquake of 9 June 1994 and the mechanism of deep-focus earthquakes, *Science, 268,* 69-73, 1995.

Stein, S., Deep earthquakes: A fault too big?, *Science, 268,* 49-50, 1995.

Tinker, M.A., W. Jiao, S.L. Beck, and T.C. Wallace, Mainshock and aftershock analysis of the June 17, 1996 deep Flores Sea earthquake sequence: Implications for the mechanism of deep earthquakes and the tectonics of the Banda Sea, *J. Geophys. Res., 103,* 9987-10,001, 1998.

van der Hilst, R., R. Engdahl, W. Spakman, and G. Nolet, Tomographic imaging of subducted lithosphere below northwest Pacific island arcs, *Nature, 353,* 37-43, 1991.

Vidale, J. E., and D. Garcia-Gonzalez, Seismic observation of a high-velocity slab 1200-1600 km in depth, *Geophys. Res. Lett., 15,* 369-372, 1988.

Vidale, J.E., and H. Houston, The depth dependence of earthquake duration and implications for rupture mechanisms, *Nature, 365,* 45-47, 1993.

Vassiliou, M.S., and H. Kanamori, The energy release in earthquakes, *Bull. Seismol. Soc. Am.*, *72*, 371-387, 1982.

Velasco, A., C. Ammon, and T. Lay, Empirical Green function deconvolution of broadband surface waves: Rupture directivity of the 1992 Landers, California, earthquake, *Bull. Seismol. Soc. Am.*, *84*, 735-750, 1994.

Wiens, D.A., and J.J. McGuire, The 1994 Bolivia and Tonga events: fundamentally different types of deep earthquakes?, *Geophys. Res. Lett.*, *22*, 2245-2248, 1995.

Wiens, D.A., J.J. McGuire, and P.J. Shore, Evidence for transformational faulting from a deep double seismic zone in Tonga, *Nature*, *364*, 790-793, 1993.

Wiens, D.A., J. McGuire, P. Shore, M. Bevis, K. Draunidalo, G. Prasad, and S. Helu, A deep earthquake aftershock sequence and implications for the rupture mechanism of deep earthquakes, *Nature*, *372*, 540-543, 1994.

Wiens, D.A., J. Hildebrand, and W. Crawford, Source and aftershock studies of the 1995 Marianas and 1996 Flores Sea deep earthquakes, *Eos Trans. AGU*, *77*(46), Fall Meet. Suppl., F491-F492, 1996.

Willemann, R.J., and C. Frohlich, Spatial patterns of aftershocks of deep focus earthquakes, *J. Geophys. Res.*, *92*, 13,927-13,943, 1987.

Zhou, H.-W., Observations on earthquake stress axes and seismic morphology of deep slabs, *Geophys. J. Int.*, *103*, 377-401, 1990.

M. Antolik, Department of Earth and Planetary Sciences, Harvard University, 20 Oxford Street, Cambridge, MA, 02138. (e-mail: antolik@seismology.harvard.edu)

D. Dreger and B. Romanowicz, Seismological Laboratory, University of California, Berkeley, CA 94720. (e-mail: dreger@seismo.berkeley.edu; barbara@seismo.berkeley.edu)